fluids

MDPI

Article

RANS Simulations of Aerodynamic Performance of NACA 0015 Flapped Airfoil

Sohaib Obeid [1,*], Ratneshwar Jha [2,*] and Goodarz Ahmadi [1,*]

[1] Mechanical & Aeronautical Engineering Department, Clarkson University, Potsdam, NY 13699, USA
[2] Aerospace Engineering, Mississippi State University, Starkville, MS 39762, USA
* Correspondence: sobied@clarkson.edu (S.O.); jha@ae.msstate.edu (R.J.); ahamdi@clarkson.edu (G.A.); Tel.: +1-315-212-4474 (S.O.); +1-662-325-2911 (R.J.); +1-315-268-2322 (G.A.)

Academic Editor: Asterios Pantokratoras
Received: 8 August 2016; Accepted: 23 December 2016; Published: 5 January 2017

Abstract: An analysis of 2D subsonic flow over an NACA 0015 airfoil with a 30% trailing edge flap at a constant Reynolds number of 10^6 for various incidence angles and a range of flap deflections is presented. The steady-state governing equations of continuity and momentum conservation are solved combined with the realizable k-ε turbulence model using the ANSYS-Fluent code (Version 13.7, ANSYS, Inc., Canonsburg, PA, USA). The primary objective of the study is to provide a comprehensive understanding of flow characteristics around the NACA 0015 airfoil as a function of the angle of attack and flap deflection at Re = 10^6 using the realizable k-ε turbulence model. The results are validated through comparison of the predictions with the free field experimental measurements. Consistent with the experimental observations, the numerical results show that increased flap deflections increase the maximum lift coefficient, move the zero-lift angle of attack (AoA) to a more negative value, decrease the stall AoA, while the slope of the lift curve remains unchanged and the curve just shifts upwards. In addition, the numerical simulations provide limits for lift increment ΔC_l and $C_{l,\max}$ values to be 1.1 and 2.2, respectively, obtained at a flap deflection of 50°. This investigation demonstrates that the realizable k-ε turbulence model is capable of predicting flow features over an airfoil with and without flap deflections with reasonable accuracy.

Keywords: aerodynamics; lift; drag; NACA 0015; flap; k-ε

1. Introduction

The aerodynamic shape of lifting objects is one of their most important design parameters. This parameter affects the amount of the lift and the drag forces that the airfoil can generate. Aircraft wings are mainly intended to provide the maximum value of the lift-to-drag ratio L/D. The L/D ratio is deemed as a measure of the efficiency of an aircraft [1] and can be stated as the amount of power (thrust) that is required to impel an aircraft of a certain weight. The aircraft wing performance is seriously impaired if flow separation occurs [2]. Commonly, flow separation results in a loss of lift, an increase of drag, diminished pressure recovery, etc. Therefore, a considerable amount of research effort has been devoted to the control of flow separation, and many methods to attain separation control have been suggested. Among the most promising active flow control approaches are suction, blowing, synthetic jet actuation and wall movement.

Proper flow control methods have the ability to reduce skin friction and form drag, increase lift and improve flight controllability. The potential benefits of flow control include enhanced range and payload, short runway landing capability, improved ecological compliance and savings in overall fuel consumption. For instance, maintaining laminar flow over the entire wing surface can reduce total aircraft drag by as much as 15% [3].

Recently, there has been considerable interest in flow control, especially in the field of aerodynamics with the intent of increasing lift and decreasing the drag of airfoils. To allow landing and take-off from short runways at reduced ground speeds, some modern airplanes are equipped with multi-element high-lift devices that generate the required high lift. Slat and single or multiple flaps are typical examples of such devices [4]. Multi-element wing designs, however, are found unfavorable from a weight and complexity point of view. That is the reason for replacing the multi-element flap with a single-hinged flap in the current designs to reduce the complexity while increasing the efficiency of the wing. While reducing the complexity of the wing, the single-hinged flap increases the chance for flow separation on the flap at large deflection angles. To prevent or at least to minimize the effects of flow separation, the air flowing over the wing near the surface must be energized so that it could overcome the effects of the adverse pressure gradient encountered along the flap.

In recent years, the possible application of trailing edge flaps as a potential vibration and noise control tool has gained considerable attention for application to the helicopter blades and wind turbines. Applications of trailing edge flap systems in helicopter rotors have been the subject of much research, both in the context of individual blade control [5], as well as smart rotor development [6–8], for the purposes of vibration reduction [9].

The employment of plain flaps in wind turbines has been also a topic of interest to many researchers. The efficacy of plain flaps in wind turbines is considered favorable both in relation to load alleviation, as well as power generation [10]. Furthermore, small flap deflections could delay the laminar-turbulent transition [11].

A wide range of engineering applications utilize airfoils operating at relatively low and medium chord Reynolds numbers ranging from 104 to 106. As noted before, helicopter rotor blades, small-to-medium-scale wind turbines and unmanned aerial vehicles are typical examples [12]. In this Reynolds number range, the boundary layer on the upper surface of an airfoil is prone to experience flow separation, even at a low incidence angle. While there is a number of published works on airfoil performance at low Reynolds numbers, still there are not many studies, either experimentally or numerically, that cover the range of Re = 10^6. In addition, despite numerous publications on the lift and drag of NACA airfoils, better understanding of airfoils with one hinged flap is still of interest [13].

Symmetric NACA airfoils with a thickness range from 9% to 18% also have many applications in industry and for demonstration purposes [14]. Gault [15] classified the stalling characteristics of the low speed NACA airfoil sections into: thin airfoil stall, leading edge stall, trailing edge stall and a combination of leading edge and trailing edge stall. Based on this classification, the NACA 0015 airfoil was selected for this study as it is classified as a medium thickness airfoil, which is susceptible only to trailing edge stall at Re = 10^6.

Numerical studies of the aerodynamic performance of the NACA 0015 airfoil with an integral-type trailing edge flap were reported by Hassan [16] using the 2D ARC2D Navier–Stokes flow solver developed at the NASA Ames Research Center. Zhang et al. [17] studied the aerodynamic performance of the NACA 0015 airfoil at different speeds using the FLUENT code. They reported the flow patterns, pressure distributions, velocity vector fields and turbulence intensities around the airfoil. Numerical studies for plain (un-flapped) airfoils were presented by Srinivasan et al. [18]. They investigated various turbulence models for unsteady flows around a NACA 0015 oscillating airfoil.

The main goal of the numerical simulations presented in this paper is to provide a thorough understanding of flow features around the NACA 0015 airfoil as a function of both angle of attack and flap deflection at Re = 10^6 by using the realizable k-ε turbulence model. The other objective is to validate the computational model by comparison of the results with the experimental data and earlier numerical simulation results. The flow problem here is of a boundary layer nature; therefore, the fluid motions near the airfoil surfaces are of interest. The Reynolds Averaged Navier–Stokes (RANS) models have been used extensively for wall-bounded flows [19]. On the other hand, many researchers consider the realizable k-ε model a suitable choice for analyzing the boundary layer flows under strong adverse pressure gradients or with separation [18].

The realizable k-ε model shares the same turbulent kinetic energy equation as the standard k-ε model, but has an improved equation for the energy dissipation term, ε, and uses a variable coefficient C_μ instead of the constant value that is used in the standard k-ε model.

The realizable k-ε model has been extensively validated for a wide range of flows [20,21]. The realizable k-ε model is found to provide more accurate predictions compared to the standard k-ε model for the cases of rotating homogeneous shear flows, free shear flows in jets and mixing layers, channel and boundary layer flows and separated flows. In addition, the realizable k-ε model properly predicts the spreading rate for axisymmetric jets, as well as that for planar jets [18].

In the present study, the 2D subsonic flows over a NACA 0015 flapped airfoil were analyzed using the realizable k-ε turbulence model of the ANSYS-Fluent (Version 13.7) computational code. The static pressure distribution, the lift and the skin friction coefficient, as well as the drag force over the flapped airfoils were studied. Attention was also given to the details of the airflow turbulence intensity distribution around the airfoil with and without flap deflection.

An analysis of the flow over the NACA 0015 airfoil with zero flap deflection is first presented. The details of the mathematical model, meshing schemes utilized and the computational analyses are described. This is followed by simulations of flapped airfoils. Validations of the computational results for cases with and without flap deflection are also presented. It is concluded that the realizable k-ε turbulence model is capable of capturing the flow conditions over the airfoils with and without flaps with reasonable accuracy.

2. Computational Modeling

2.1. Formulation

In this study, the ANSYS-Fluent (Version 13.7) code is used as the solver along with the realizable k-ε turbulence model for solving the Reynolds Average Navier–Stokes (RANS) equations for flow around the NACA 0015 airfoil with and without a hinged flap. The code solves the equations of the conservation of mass and balance of momentum. Additionally, the transport equations are also solved for turbulence properties. The realizable k-ε model has the following transport equations [20]

$$\frac{\partial}{\partial t}(\rho k) + \frac{\partial}{\partial x_j}(\rho k u_j) = \frac{\partial}{\partial x_j}\left[(\mu + \frac{\mu_t}{\sigma_k})\frac{\partial k}{\partial x_j}\right] + P_k + P_b - \rho\varepsilon - Y_M + S_k \tag{1}$$

$$\frac{\partial}{\partial t}(\rho \varepsilon) + \frac{\partial}{\partial x_j}(\rho \varepsilon u_j) = \frac{\partial}{\partial x_j}\left[(\mu + \frac{\mu_t}{\sigma_\varepsilon})\frac{\partial \varepsilon}{\partial x_j}\right] + \rho C_1 S\varepsilon - \rho C_2 \frac{\varepsilon^2}{k + \sqrt{\gamma\varepsilon}} + C_{1\varepsilon}\frac{\varepsilon}{k}C_{3\varepsilon}P_b + S_\varepsilon \tag{2}$$

where $C_1 = \max\left[0.43 + \frac{\eta}{\eta+5}\right]$, $\eta = S\frac{k}{\varepsilon}$, $S = \sqrt{2S_{ij}S_{ij}}$.

In these equations, P_k represents the generation of turbulence kinetic energy due to the mean velocity gradient. P_b is the generation of turblence kinetic energy due to buoyancy. The turbulent eddy viscosity is given as $\mu_t = \rho C_\mu \frac{k}{\varepsilon}^2$, where $C_\mu = \frac{1}{A_o + A_s\frac{kU^*}{\varepsilon}}$, $U^* \equiv \sqrt{S_{ij}S_{ij} + \check{\Omega}_{ij}\check{\Omega}_{ij}}$, $\check{\Omega}_{ij} = \Omega_{ij} - 2\varepsilon_{ijk}\omega_k$, $\Omega_{ij} = \overline{\Omega}_{ij} - \varepsilon_{ijk}\omega_k$. Here, $\overline{\Omega}_{ij}$ is the mean rate of the rotation tensor viewed in a rotating reference frame with the angular velocity ω_k. The model constants A_o and A_s are given as: $A_o = 4.04$, $A_s = \sqrt{6}\cos\phi$, where $\phi = \frac{1}{3}cos^{-1}\left(\sqrt{6}W\right)$, $W = \frac{S_{ij}S_{jk}S_{ki}}{\tilde{S}^3}$, $\tilde{S} = \sqrt{S_{ij}S_{ij}}$, $S_{ij} = \frac{1}{2}\left[\frac{\partial u_j}{\partial x_i} + \frac{\partial u_i}{\partial x_j}\right]$; and the model constants are: $C_{1\varepsilon} = 1.44$, $C_2 = 1.9$, $\sigma_k = 1.0$ and $\sigma_\varepsilon = 1.2$.

2.2. Evaluation of C_p, C_l and C_f

The pressure coefficient, C_p, and the lift coefficient, C_l, are evaluated as,

$$C_p = \frac{p - p_\infty}{q_\infty} \tag{3}$$

$$C_l \approx \int_0^1 \left[[C_p]_{\text{Pressure Side}} - [C_p]_{\text{Suction Side}} \right] d\left(\frac{x}{c}\right) \quad (4)$$

In these equations, p is the surface static pressure; p_∞ is the free stream static pressure; q_∞ is the free stream dynamic pressure, which is defined as $q_\infty = \frac{1}{2}\rho v_\infty^2$; and x/c is the normalized chord-wise position. The skin friction coefficient C_f is the ratio of the surface shear stress, τ, to freestream dynamic pressure. That is,

$$C_f = \frac{\tau}{q_\infty} \quad (5)$$

2.3. Computational Domain and Boundary Conditions

To facilitate the grid generation process, as well as the analysis, similar to the earlier study of Hassan [16], the airfoil with the deflected trailing edge flap is treated as a single-element airfoil with no gap between the flap's leading edge and the base of the forward portion of the airfoil. For deflecting the flap, solid body rotations were assumed, and a four-point spline smoothing was made for the resulting airfoil at the chord-wise position corresponding to the location of the flap hinge point. Figure 1 shows the schematic geometry of the NACA 0015 with various trailing edge flap deflections.

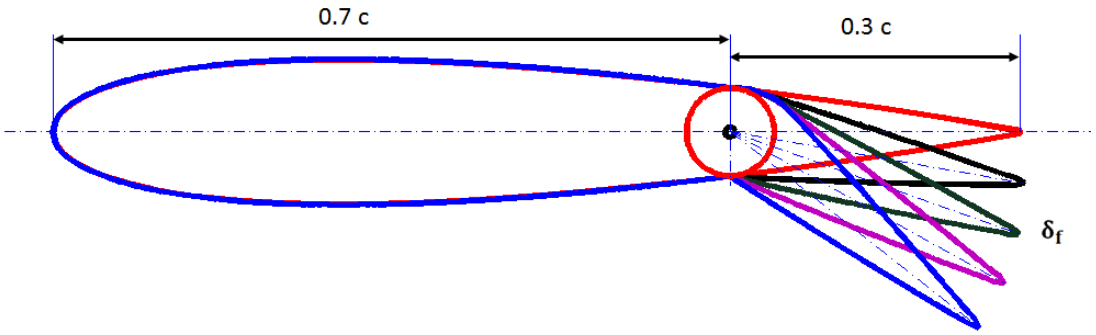

Figure 1. Geometry of the NACA 0015 airfoil with a 30% trailing edge deflected flap.

To develop a high efficiency simulation, a C-structured grid topology of a semi-elliptical shape with semi-major diameter 43.5 c and semi-minor diameter 10 c, where c is the chord length, was generated using the preprocessor Gambit (Version 2.4.6, ANSYS, Inc., Canonsburg, PA, USA). The elliptic shape of the grid provides major advantages over other conventional shapes, such as rectangular and semicircle upstream and rectangular downstream. The main advantage is providing flexibility in using the same mesh for different angles of attack by only shifting the tail part of the mesh at the airfoil trailing edge in accordance with the specific angle of attack. For this purpose, it is made sure that the edge of the elliptic domain has sufficient vertical length to contain the incoming flow for angles of attack up to 20°. The approach also leads to considerable reduction in the needed number of cells in the mesh in the far-field; thus allowing for the majority of the cells in the mesh to be concentrated around the airfoil [22].

The distance of the rear pressure far field from the airfoil is 30 c, and the majority of the cells are clustered toward the airfoil surface. This sufficiently large domain was chosen to cover flow disturbances created by the airfoil and avoid unphysical reflections from the outer edges of the grid. The schematic of the computational domain and mesh around the airfoil is shown in Figure 2.

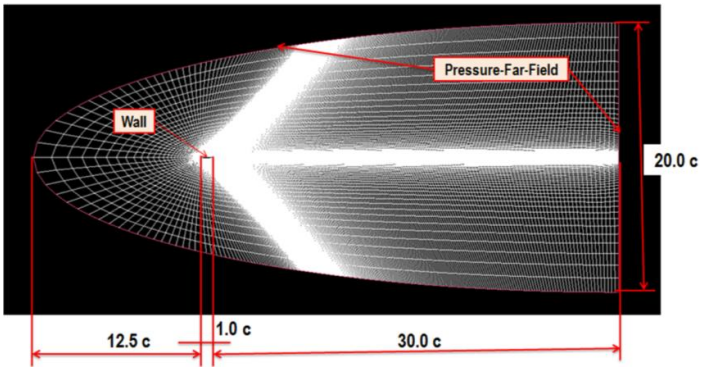

Figure 2. Domain of calculations and boundary conditions.

The grids constructed for this study have about 104,000 cells with a four-node quadrilateral element. To simulate the wake area correctly, Dolle [22] recommended using a fine grid with quadrilateral cells in these areas rather than other type of cells. Therefore, refined quadrilateral cells were placed on top of the boundary layer grid on the upper side and lower side of the airfoil outline. Figure 3 shows the details of the structured mesh, which is highly clustered toward the airfoil surface, and it is fine in the vicinity of wake regions and deflected flaps.

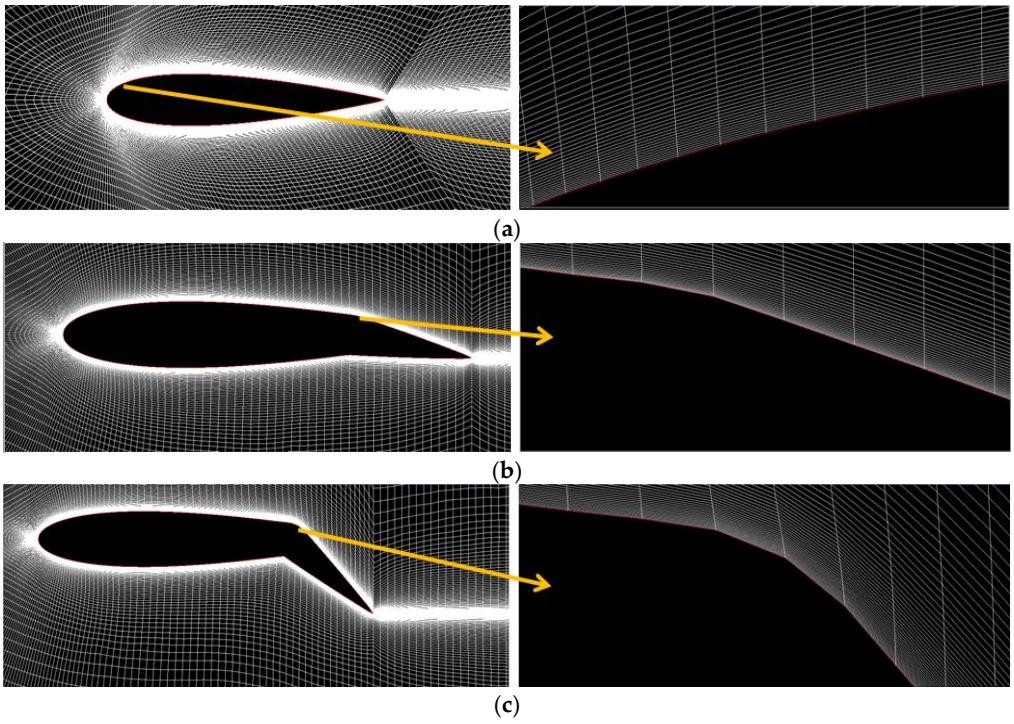

Figure 3. Mesh clustering toward airfoil surface and deflected flap regions. (**a**) Airfoil with 0° flap deflection; (**b**) airfoil with 10° flap deflection; (**c**) airfoil with 40° flap deflection.

The boundary conditions for this simulation were the pressure far-field at the computational domain periphery and stationary wall condition at the airfoil surface. The pressure far-field boundary is a non-reflecting boundary condition based on "Riemann invariants" used to model a free-stream condition at infinity, with the free-stream Mach number and static conditions being specified. At the wall, the standard wall function boundary condition was used. The calculation procedures at the pressure far-field boundaries, as well as the shear-stress calculations at wall boundaries were described in the Fluent lecture notes [23]. In some cases, the mesh is adapted based on the static pressure gradient,

using the default mesh adaptation control settings, so the solver periodically refines the mesh in the regions of high pressure gradients.

2.4. Setting up of the Numerical Simulation Parameters

Time independent pressure-based solver is used within ANSYS-Fluent (Version 13.7) for the analysis. The realizable k-ε turbulence model is selected for analyzing the boundary layer flow over the airfoil. The airflow is assumed to be incompressible. A simple scheme with the Green-Gauss cell-based gradient implicit formulation of pressure velocity coupling is utilized [23]. For spatial discretization, the second order upwind differencing scheme which offers several advantages over a central-differencing formulation for computing viscous flows is used in this work [24]. The ANSYS-Fluent code solves the coupled governing equations of fluid motion simultaneously and provides updating correction for the pressure value in each iteration [25]. A convergence criterion of 1×10^{-8} was used for the continuity, x-velocity, y-velocity, k and ε. All solutions converged with the standard interpolation scheme for calculating cell-face pressure and second order up-wind density, momentum, turbulent kinetic energy, turbulent dissipation rate and energy interpolation schemes for turbulent flow.

3. Results and Discussion

3.1. Mesh Independence Tests

To ensure that the simulation results are independent of grid size, different computational meshes were inspected. This is done by running cases with increasing number of grid cells until the simulation results did not change with the use of progressively finer grids. Table 1 lists the properties of six different grids with varying density that have been inspected for the flow pattern around the NACA 0015 airfoil with zero flap deflection. This table lists some details of the grids, including the total number of cells, the number of nodes N_x and N_y placed, respectively, in the x and y directions and the maximum, minimum and average values of non-dimensional normal distance from the wall, y^+, for each grid. It is observed that all of the grids inspected have considerably low y^+ values, particularly Grids III–VI, to sufficiently resolve the viscous sub-layer.

Table 1. Details of grids used in mesh sensitivity testing.

Grid	No. of Cells	N_x	N_y	Max y^+	Min y^+	Aver y^+
I	24,910	690	35	32.5	4.8	13.85
II	53,040	884	50	16.5	3.4	06.55
III	76,128	976	65	12	1	05.50
IV	103,192	1184	75	9.2	0.8	04.20
V	141,168	1384	85	8.8	0.7	04.05
VI	367,235	1850	90	1.01	0.01	0.500

Table 2 provides more details on the distribution of cells for different inspected meshes along the x and y directions. To have a better control of the distribution of the mesh, the airfoil body was divided into two parts; the front portion of the airfoil, which extends from the leading edge up to 30% of the chord length, and the rear portion of the airfoil, which includes the rest of the airfoil body. The wake region extends from the airfoil trailing edge up to the right far-field end. In each case, the first 30% of the airfoil was meshed with non-uniform grid spacing along the x-axis, while the last 70% of the airfoil meshed with uniform grid spacing. The number of grid cells located in the airfoil rear portion is more than three-times that located at the front part.

Table 2. Details of the grid cells distribution along the x-axis and y-axis.

Grid	Leading Edge up to 30% of Chord	Trailing Edge up to 70% of Chord	Wake Region	Height
I	90	325	275	35
II	110	374	400	50
III	112	384	480	65
IV	116	468	600	75
V	120	544	720	85
VI	128	597	1125	90

The mesh size near the airfoil surface is a critical parameter for proper simulation of boundary layer flow properties. The size of the first cell height near the wall Δy was estimated based on the physical properties of the fluid used and the selected values of the non-dimensional normal distance from the wall y^+. Table 3 gives values for estimated size of this first cell height as a fraction of airfoil chord length. The mesh growth factor that controls the transition of cell size and specifies the increase in element size for each succeeding layer is found to be 1.2.

Table 3. Estimated size of the first cell height near the wall as a fraction of airfoil chord length.

Grid	Max y^+	Min y^+	Aver y^+	Max Δy	Min Δy	Aver Δy
I	32.5	4.8	13.85	$7.65 \times 10^{-4}\ c$	$1.00 \times 10^{-4}\ c$	$3.17 \times 10^{-4}\ c$
II	16.5	3.4	6.55	$3.78 \times 10^{-4}\ c$	$7.80 \times 10^{-5}\ c$	$1.50 \times 10^{-4}\ c$
III	12	1	5.50	$2.75 \times 10^{-4}\ c$	$2.30 \times 10^{-5}\ c$	$1.26 \times 10^{-4}\ c$
IV	9.2	0.8	4.20	$2.11 \times 10^{-4}\ c$	$1.83 \times 10^{-5}\ c$	$9.93 \times 10^{-5}\ c$
V	8.8	0.7	4.05	$2.02 \times 10^{-4}\ c$	$1.60 \times 10^{-5}\ c$	$9.27 \times 10^{-5}\ c$
VI	1.01	0.01	0.500	$2.38 \times 10^{-5}\ c$	$2.35 \times 10^{-7}\ c$	$1.18 \times 10^{-5}\ c$

In this section, the grid inspection studies for flows at Reynolds numbers of 10^5 and 10^6 are performed. The results of the two-equation realizable k-ε model of Shih et al. [20] were compared with those of the one-equation closure model of the Spalart–Allmaras (SA). The SA model was developed mainly for simulating aerodynamic flows. This model solves the modeled transport equation for the kinematic eddy (turbulent) viscosity [26]. The results obtained from SA and R-k-ε numerical models were compared with the experimental data of Rethmel [27]. Tables 4 and 5 show the predicted values of the lift coefficients for six different meshes by using the Spalart–Allmaras (SA) and the R-k-ε turbulence models for Re = 10^5 and 10^6, respectively. It is apparent that the realizable k-ε solutions obtained by Grids IV, V and VI are in good agreement with the experimental data. Despite the fact that the number of cells in Grid VI is approximately 3.7-times that of Grid IV, these grids provided nearly the same results for the lift coefficient. It is also seen that the SA model yields significantly higher C_l values compared to the experiments. Regardless of the turbulence model used, the numerical results for these last three grids remain almost the same with increasing the number of cells from Grid IV–Grid VI.

Table 4. Lift coefficient values for the NACA 0015 airfoil at $\alpha = 12°$, $\delta = 0°$ and Re = 10^5 using RANS models. SA, Spalart–Allmaras.

Grid	C_l Exp.	C_l (R-k-ε Model)	C_l (SA Model)
I	0.90 ± 0.005	0.7654	0.9845
II	0.90 ± 0.005	0.8292	1.0276
III	0.90 ± 0.005	0.8412	1.0988
IV	0.90 ± 0.005	0.9091	1.1169
V	0.90 ± 0.005	0.9016	1.1199
VI	0.90 ± 0.005	0.9073	1.1178

Table 5. Lift coefficient values for the NACA 0015 airfoil at $\alpha = 12^\circ$, $\delta = 0^\circ$ and $Re = 10^6$ using RANS models.

Grid	C_l Exp.	C_l (*R-k-ε* Model)	C_l (SA Model)
I	1.12 ± 0.005	8.546×10^{-1}	1.0034
II	1.12 ± 0.005	9.655×10^{-1}	1.1642
III	1.12 ± 0.005	9.891×10^{-1}	1.2521
IV	1.12 ± 0.005	1.1463	1.316
V	1.12 ± 0.005	1.1491	1.3230
VI	1.12 ± 0.005	1.1484	1.3201

The last step in the grid convergence inspection was focused on the analysis of the distribution of the pressure coefficient along the airfoil chord, as well as the velocity profiles on the upper surface of the airfoil in some selected sections. Figure 4 presents the chordwise distributions of the pressure coefficient (C_p) profile for the airfoil predicted by Grids I, IV and VI using the *R-k-ε* turbulence model for $\alpha = 12^\circ$, $\delta = 0^\circ$ and $Re = 10^5$ (a) and $Re = 10^6$ (b). Here, the predicted distributions of the pressure coefficient are compared with the experimental data of Rethmel [27]. It is seen that the model predictions for the pressure coefficient are generally comparable with the experimental data. In particular, the predictions obtained by Grids IV and VI are very close to each other and to the distribution of the experimental data for both Reynolds numbers.

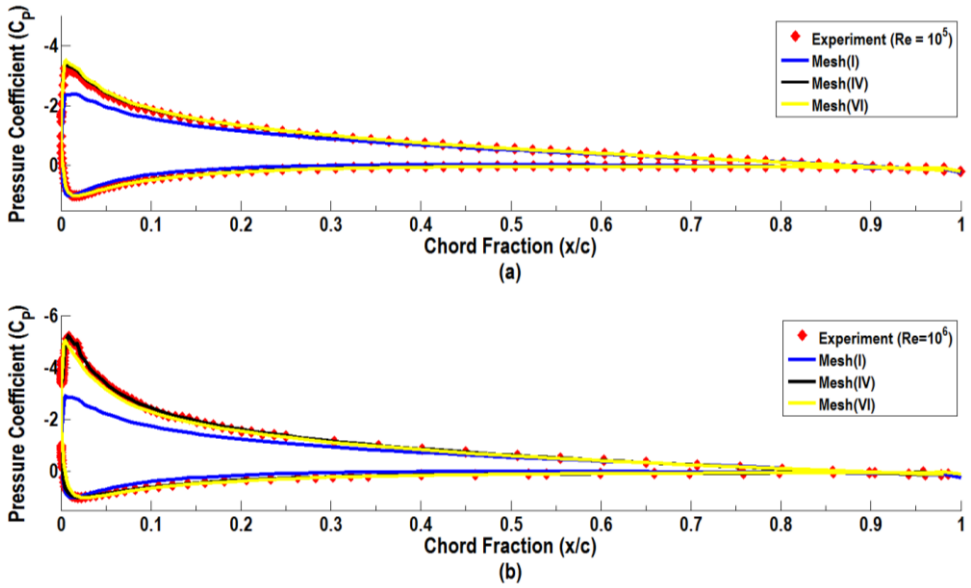

Figure 4. Comparison of pressure coefficient curves along the sides of airfoil from different grids at $\alpha = 12^\circ$ and $\delta = 0^\circ$ with the experimental data of Rethmel [27] at (**a**) $Re = 10^5$ and (**b**) $Re = 10^6$.

Figure 5 shows the velocity profiles on the upper surface of airfoil at the 20% cord location from the leading edge as predicted by the realizable *k-ε* model using Grids I, IV and VI for $\alpha = 12^\circ$ and $\delta = 0^\circ$ for $Re = 10^5$ and $Re = 10^6$. The vertical axis (y) in Figure 5 denotes the vertical distance from the surface of the airfoil as a fraction of the chord length. It is seen that the model predictions for Grids IV and VI are almost identical. That is, further refinement of Grid IV does not have a noticeable effect on the velocity profile.

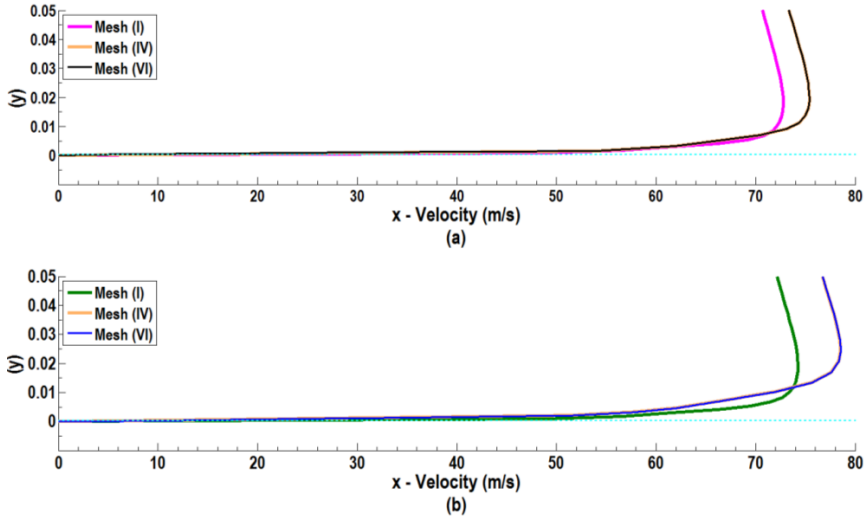

Figure 5. Velocity profiles on the upper surface of airfoil at a 20% cord location from the leading edge at $\alpha = 12^\circ$ and $\delta = 0^\circ$ and for (**a**) Re = 10^5 and (**b**) Re = 10^6.

The presented grid sensitivity analysis shows that the model predictions with the use of Grids IV and VI are very close to each other and to the experimental data. Due to the high computational cost associated with the use of Grid VI, Grid IV with a total number of 103,192 cells was used in the subsequent analyses.

3.2. NACA 0015 Airfoil with Zero Flap Deflection

The airflow properties around the NACA 0015 with zero flap deflection are first studied, and the corresponding distributions of static pressure and velocity magnitude at different incidence angles are evaluated and compared with the published numerical results and/or experimental data.

Figure 6 shows the static pressure and velocity magnitude contours around the NACA 0015 airfoil for a few selected incidence angles. As NACA 0015 is a symmetric airfoil, at zero incidence angle, the static pressure and velocity distribution over the airfoil are symmetric, which results in zero lift force and a stagnation point, exactly at the nose of the airfoil. There are regions of accelerated flows over and under the airfoil that reach the highest speed at the airfoil maximum thickness point. The velocity is high (marked by red spots) in the low pressure region and vice versa. The maximum pressure occurs at the stagnation point when the velocity is zero.

At an incidence angle of 5°, the contours of static pressure over the airfoil become asymmetric; the pressure on the upper surface becomes lower than the pressure on the lower surface; regions of high pressure on the airfoil lower surface become dominant; and a lift coefficient of 0.531 is generated due to the pressure imbalance.

Figure 6 shows that as the angle of attack increases, the stagnation point is shifted towards the trailing edge on the bottom surface; hence, it creates a low velocity region at the lower surface of the airfoil and a high velocity region on the upper side of the airfoil. Thus, the pressure on the upper side of the airfoil is lower than the ambient pressure, whereas the pressure on the lower side is higher than the ambient pressure. Therefore, increasing the incidence angle is associated with the increase of the lift coefficient, as well as the increase of the drag coefficient. This increase in the lift coefficient continues up to a maximum, after which the lift coefficient decreases.

It is also seen that the flow field around the airfoil varies markedly with the incidence angle. In addition to the changes in velocity and pressure distributions, the properties of the boundary layer flow along the airfoil surface also change. At low incidence angles up to about 12°, the boundary layer is fully attached to the surface of the airfoil, and the lift coefficient increases with angle of attack, while the drag is relatively low. With the increase of incidence angle, the boundary layer is thickened.

When the incidence angle of the airfoil is increased to about 13° or larger, the adverse pressure gradient imposed on the boundary layers become so large that separation of the boundary layer occurs. A region of recirculating flow over the entire upper surface of the airfoil forms, and the region of higher pressure on the lower surface of the airfoil becomes smaller. Consequently, the lift decreases markedly, and the drag increases sharply. This is a typical condition in which the airfoil is stalled.

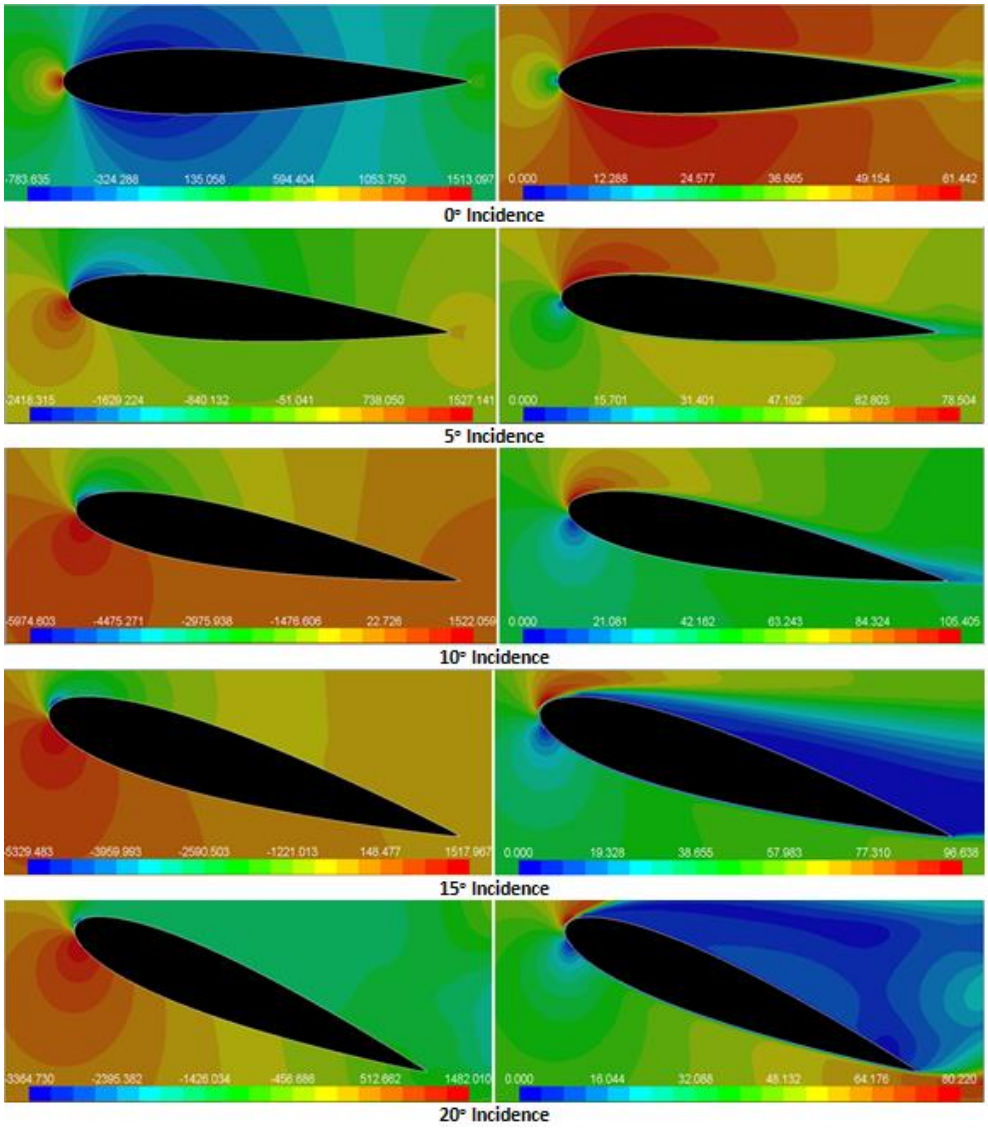

Figure 6. Static pressure and velocity magnitude contours around the NACA 0015 airfoil at different incidence angles.

For a further increase of the airfoil incidence angle to 20°, the stagnation point shifts significantly further towards the trailing edge on the bottom surface. The recirculating flow region becomes dominant and covers the entire upper surface of the airfoil, and the airflow is fully separated from the upper surface of the airfoil. This leads to further reduction of the lift force and a severe increase of the drag force.

The air flowing along the top of the airfoil surface experiences a change in pressure, moving from the ambient pressure in front of the airfoil, to a lower pressure over the surface of the airfoil, then back to the ambient pressure behind the airfoil. The region where fluid must flow from low to high pressure (adverse pressure gradient) could cause flow separation. If the adverse pressure gradient is too high, the pressure forces overcome the fluid inertial forces, and the flow separates from the airfoil

upper surface. As noted before, the pressure gradient increases with incidence angle, and there is a maximum angle of attack for keeping the flow attached to the airfoil. If the critical incidence angle is exceeded, separation occurs, and the lift force decreases sharply.

Figure 7 shows how the predicted position of the stagnation point varies for different angles of attack. It is apparent that with positive angle of attack (AoA) the stagnation point moves toward the trailing edge on the lower surface of the airfoil, while this movement would be on the upper surface of the airfoil at negative angles. The variation of the stagnation point position with the angle of attack obtained in this study is compared with the results obtained by Ahmed et al. [28] for the NACA 0012 airfoil. Although the NACA 0012 airfoil is thinner, the present results match well up to an AoA of 12° and then follow the same trend.

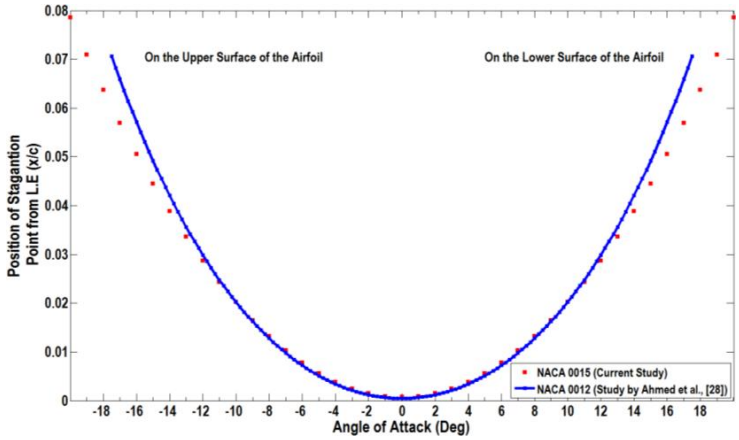

Figure 7. Variation of the stagnation point position with the angle of attack.

Figure 8 presents the chordwise distributions of the pressure coefficient (C_p) profile for the airfoil at some selected incidence angles. For small angles of attack, the C_p distribution is characterized by a negative pressure peak near the leading edge on the suction side. Beyond this point, the C_p value gradually increases along the chord of the airfoil. On the pressure side of the airfoil, the C_p value reaches a maximum of $C_p = 1$ at the stagnation line. This point is near the leading edge, but shifts slightly depending on the incidence angle. Further down the chord length of the airfoil, the pressure side C_p value increases gradually until it equals the suction side value at the trailing edge.

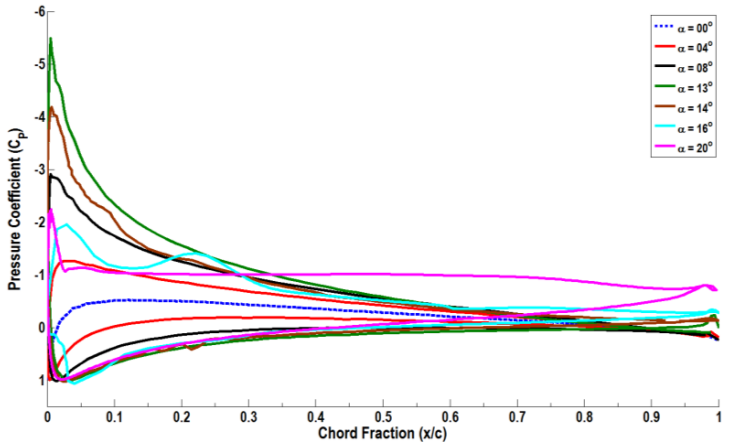

Figure 8. Pressure coefficient curves along the upper and lower surfaces of the airfoil with 0° flap deflection for different incidence at Re = 10^6.

Figure 8 also shows that the flow remains attached to the suction surface up to $\alpha = 13^\circ$ after which flow begins to separate. The separation line starts near the trailing edge and moves forward toward the leading edge as incidence increases. The flow becomes fully separated over almost the entire chord of the airfoil for α greater than 15°. For $\alpha > 13^\circ$, the maximum C_p negative value decreases on the airfoil upper side, and a pronounced shift of the stagnation position toward the trailing edge is found. This situation continues until $\alpha = 17^\circ$, at which the C_p value starts to vary in an irregular manner.

For better understanding of the airflow characteristics around the airfoil, variations of the skin friction coefficient are evaluated for selected incidence angles, as shown in Figure 9. The skin friction coefficients increase with the incident angle and also show a smooth variation for angles of attack equal to or smaller than 13°. The skin friction coefficient curve at $\alpha = 16^\circ$ shows an irregular variation, which is a typical trend for the cases when there are some separation zones.

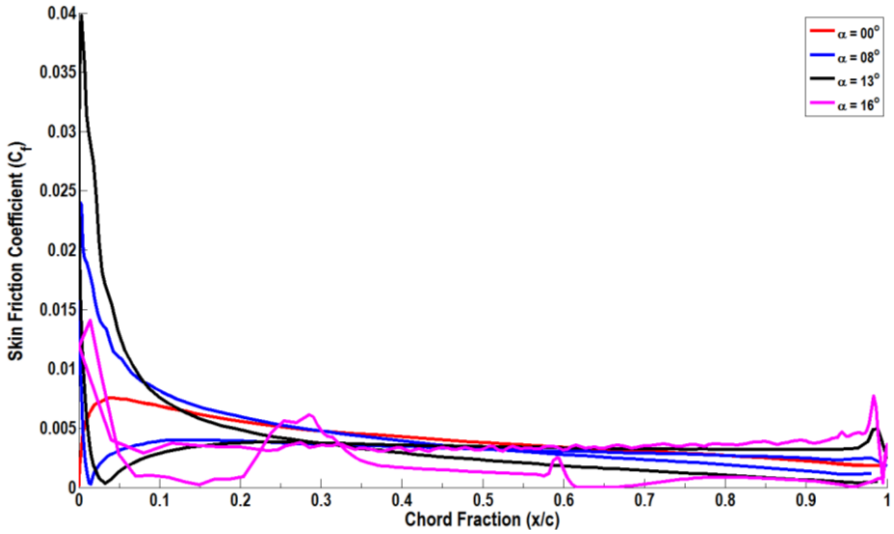

Figure 9. Skin friction coefficient curves along the airfoil with 0° flap deflection for different incidence angles at Re = 10^6.

Figure 10 shows the variation of the lift coefficient with the incidence angle at free stream conditions corresponding to a chord Reynolds number of 10^6. The lift and drag coefficients from the ANSYS-Fluent RANS simulations were calculated, and the results for the lift coefficient are shown in this figure. It is seen that the lift coefficient increases with the angle of attack up to about 13° and then decreases. The lift coefficient obtained from 2D potential flow analysis using the panel method, the RANS simulation results of Joslin et al. [29] and the large eddy simulation results of You and Moin [2] are also shown in this figure for comparison. In addition, the experimental data of Rethmel [27] for the NACA 0015 at chord Re = 10^6 and the data of Lasse and Niels [30] at a chord Re of 1.6×10^6 are also reproduced in Figure 10. It should be pointed out that the potential flow solution that treats the flow around the airfoil as inviscid and irrotational is an idealized case for extremely high Reynolds number flows [31].

It is seen that the lift coefficient increases with the incidence angle up to $\alpha = 13^\circ$, after which lift starts to decrease. The present RANS-realizable k-ε turbulence model simulation results are in general agreement up to the point of separation with earlier RANS results of Joslin et al. [29], Large Eddy Simulation (LES) results of You and Moin [2] and the experimental data of Rethmel [27] and Lasse and Niels [30]. After the point of separation, the current RANS predictions are in general agreement with the experimental data of Rethmel [27], as well as the LES results of You and Moin [2]. The RANS simulations of Joslin et al. [29] that use the one-equation Spalart–Allmaras turbulence model, however, over-predict the LES and the experimental data.

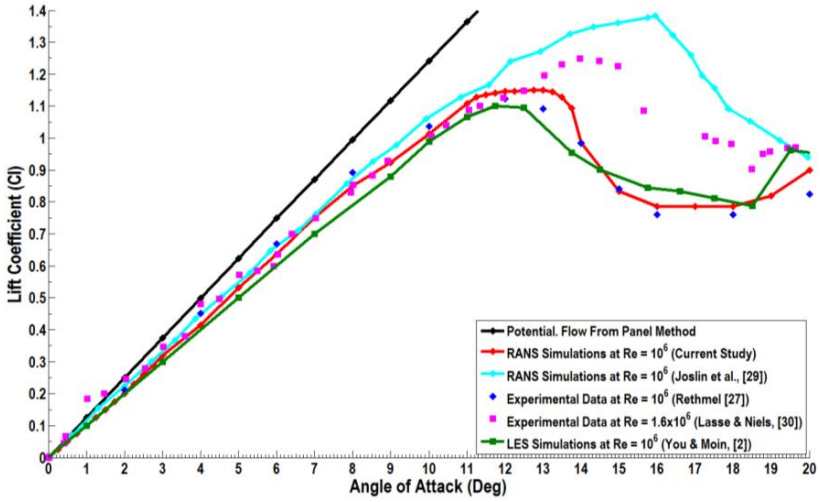

Figure 10. Comparison of lift coefficient C_l values of the airfoil at 0° flap deflection as a function of (α) at chord Re = 10^6 with experimental and numerical results.

While the present RANS simulations for the lift coefficient are in good agreement with the experimental data of Rethmel [27], the matching of the integrated lift coefficients does not necessarily ensure agreement in the pressure distribution around the airfoil. Figure 11a shows the chord-wise distribution of pressure coefficient C_p on the airfoil as predicted by the present RANS simulation at the onset of stall (α = 12°). The experimental data of Rethmel [27] are reproduced in this figure for comparison. Excellent agreement in the chord-wise distributions of the predicted pressure coefficient with the experimental data is seen from this figure. This emphasizes the observation that the realizable k-ε turbulence model provides an accurate description of the pressure distribution around the airfoil at this incidence angle.

For angles of incidence in the stalled regime (α > 13°), the flow separation occurs, and the accuracy of the realizable k-ε turbulence model in predicting the separated flow structures becomes somewhat questionable. In fact, a careful examination of Figure 10 reveals that the k-ε turbulence model slightly over-predicts the experimental lift coefficient at high angles of attack of α = 13°–14°. To examine this trend, Figure 11b shows the distribution of C_p as predicted from the current RANS simulation at the fully-developed stall regime (α = 16°) and compares them with the experimental data of Rethmel [27]. There are noticeable differences between these pressure distributions.

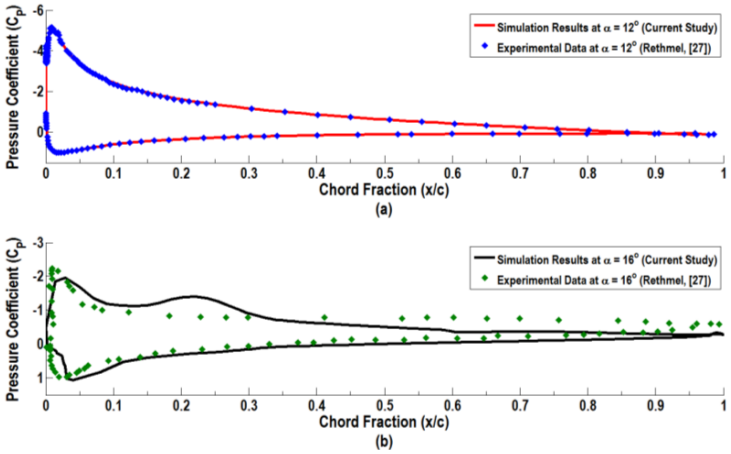

Figure 11. Comparison of predicted pressure coefficients around the airfoil at angle of attack (AoA) = 12° and AoA = 16° with the experimental data of Rethmel [27].

It is worth mentioning that the maximum lift coefficient predicted by the present simulations is 1.15 for $\alpha = 13^\circ$. The slope of the lift curve obtained from the current study, as well as those for the earlier numerical results and experimental data is $\frac{\partial C_l}{\partial \alpha} = 0.101$ for low AoA, which remains constant for incidence angles up to about 11°. The slope of the lift curve is $\frac{\partial C_l}{\partial \alpha} = 0.11$ for the potential flow case.

Figure 12 exhibits the predicted variation of drag coefficients with the incidence angles and provides comparison with the earlier RANS simulations and the experimental data. As expected, the drag coefficient increases with the increase of incidence angle. The RANS simulation results of Schroeder [32] for the NACA 0012 airfoil at Re = 10^6 and the drag coefficient measurements' data of Sharma [33] for the NACA 0015 at Re = 0.7×10^6 are reproduced in this figure for comparison. In addition, the drag coefficient data of Sheldahl and Klimas [34] for the NACA 0015 at Re = 10^6 and those of Lasse and Niels [30] at Re = 1.6×10^6 are also shown in this figure. It is seen that the drag coefficient values predicted by the realizable k-ε model are in reasonable agreement with the experimental data and earlier numerical results for incident angle less than 13°. The drag coefficient is low at zero incidence angles and increases slowly with the angle of attack to the value of 0.038 at the stall condition. The slope of the drag coefficient with respect to incidence angle, $\frac{\partial C_d}{\partial \alpha}$, remains roughly constant at about 0.003. After the stall condition, the drag coefficient increases rapidly with the further increase of the angle of attack and reaches a value of 0.28 at $\alpha = 20^\circ$, which is more than seven-times the drag coefficient at the stall condition. The slope of the drag coefficient versus incidence angle, $\frac{\partial C_d}{\partial \alpha}$, jumps to a value of 0.04 after the stall condition. It is also seen that the value of the drag coefficient decreases with the increase of the Reynolds number. It is also observed that for an incident angle beyond separation, the present model overestimates the experimental data for the drag coefficient. Further study of the accuracy of various turbulence models including the realizable k-ε turbulence model are left for a future work.

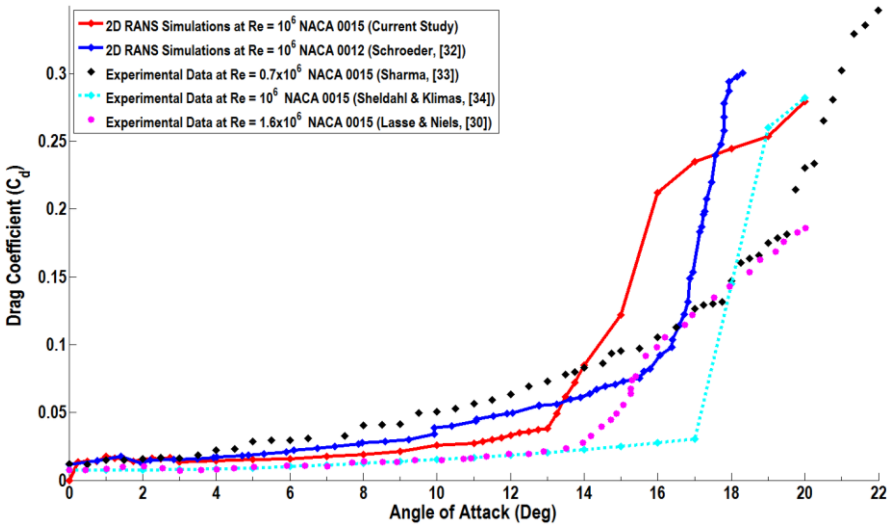

Figure 12. Comparison of drag coefficient of airfoil at 0° flap deflection versus angle of attack at chord Reynolds number Re = 10^6 with the experimental data and earlier numerical results.

Figure 13 shows the variation of the lift-to-drag ratio (C_l/C_d) with the incidence angle as predicted by the realizable k-ε model and the comparison with the available experimental data and earlier simulations. It is seen that the lift-to-drag ratio increases rapidly from zero at $\alpha = 0^\circ$ toward its maximum value with the increase in incidence angle. This is because for small angles of attack, both C_l and C_d increase, but C_l increases faster than C_d [35]. Then, as the angle of attack further increases, the lift-to-drag ratio decreases, and the decreasing trends are continuous to beyond the stall angle.

While the trend of variations of the lift-to-drag ratio of the present simulations is in qualitative agreement with the experimental data and earlier simulations, there are quantitative differences in the peak value of this ratio. The maximum value of lift-to-drag ratio found for the present simulations is 48.2, which occurs at AoA of 8.5°. Figure 13 shows that the maximum value of lift-to-drag ratio for most cases occurs at AoA of 8°–8.5°, except for the data of Sheldahl and Klimas [34], for which the peak occurs at AoA of 10°. This figure also shows that the lift-to-drag ratio could reach a peak value of about 65.

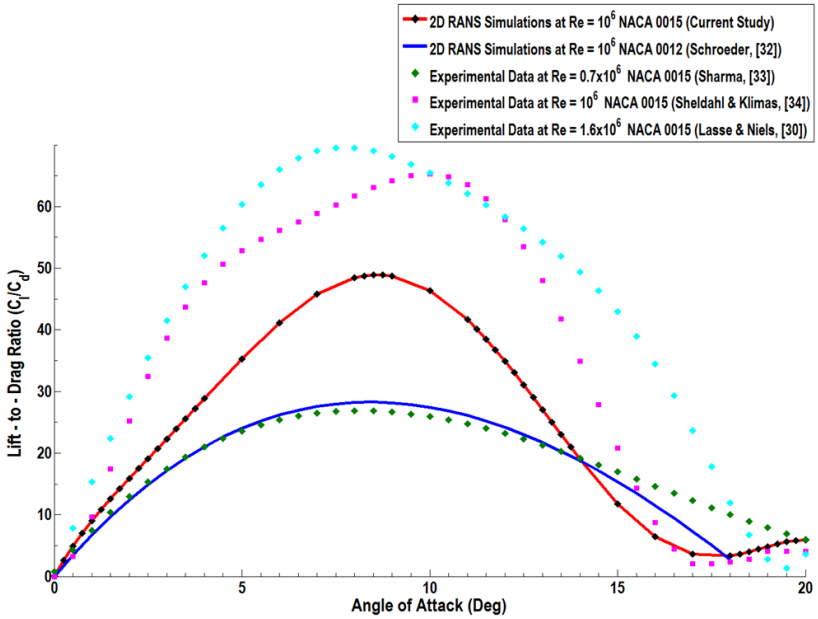

Figure 13. Comparison of the lift-to-drag C_l/C_d ratio of the airfoil at 0° flap deflection versus the angle of attack at chord Re = 10^6 with experimental data and earlier numerical results.

Another result obtained from this study is the behavior of the turbulence intensity of the flow around the airfoil. Here, the turbulence intensity (TI) is defined as the ratio of root mean square velocity fluctuation u', to the mean local flow velocity U_{aver} (Fluent lecture notes [23]). Figure 14 shows the turbulence intensity contours around the airfoil for selected incidence angles as a percentage. It is seen that the turbulence level increases with incident angle and could reach a maximum of 49% for the range of incidence angles considered. At zero incidence angle, the maximum turbulence intensity occurs near the leading edge of the airfoil. At an incidence angle of 5°, the contour map of turbulence intensity shows a slight shift of the location of the maximum intensity region toward the trailing edge on the upper surface of the airfoil.

Figure 14 also indicates that at low incidence angles up to about 12°, a turbulent boundary layer is attached to the airfoil, and only a thin wake is formed behind the airfoil. When the airfoil incidence angle is increased to 13° or larger (where the flow separation is expected to occur), the wake becomes much larger, and the region with maximum turbulent intensity becomes larger and departs further from the airfoil surface. For the airfoil incidence angle of 20°, the airfoil is passing through a deep stall, where the airflow on its upper surface separates right after the leading edge and produces a wide wake. In this case, the maximum turbulence intensity region occupies a large zone off the airfoil surface, but close to the trailing edge.

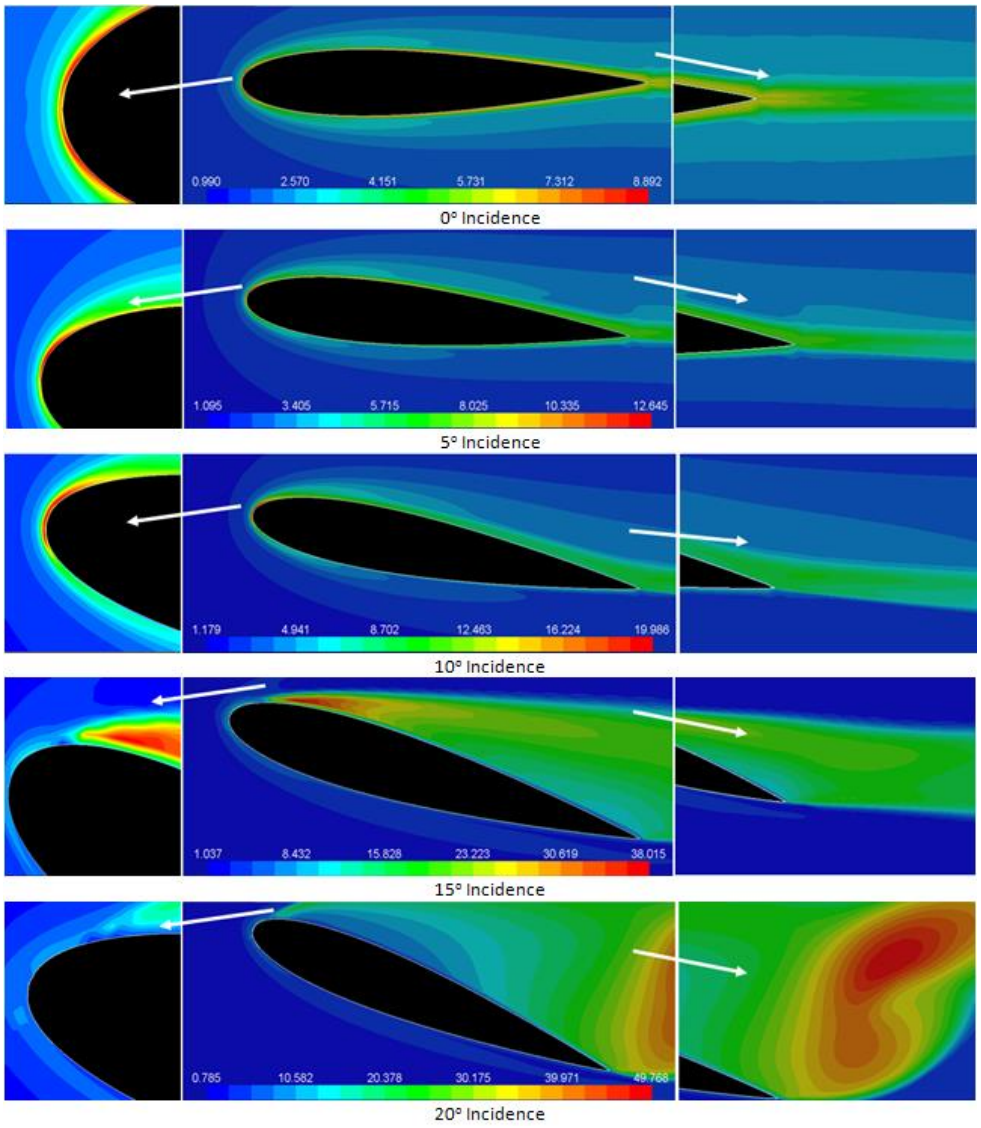

Figure 14. Turbulence intensity contours (%) for flow around the airfoil at various incidence angles. Enlarged views of certain regions are shown on the contours on the left and right for clarity.

Table 6 lists the predicted maximum turbulence intensities as a percent for several incidence angles. The simulation results of Zhang et al. [17] for airflow around the NACA 0015, who used the k-ω model at Re= 0.55×10^6, are also reproduced in this table for comparison. It is seen that the results of the present realizable k-ε model for the peak turbulence intensity are in qualitative agreement with those reported by Zhang et al. [17]. Table 6 also shows the expected increasing trend of turbulence intensity with the angle of incidence.

Table 6. Comparison of the maximum turbulence intensity (TI) at different incidence angles with the results of Zhang et al. [17].

AoA	Maximum TI (%) Current Study	Maximum TI (%) Zhang et al. [17]
0°	8.892	13.95
5°	12.645	18.04
10°	19.986	28.75
15°	38.015	42.11
20°	49.768	51.20

3.3. NACA 0015 Airfoil with Flap Deflection

The effect of downward flap deflection on the aerodynamic performance of the airfoil is studied for eight different flap positions of 2°, 5°, 10°, 15°, 20°, 25°, 30° and 40°. For zero AoA, the static pressure and velocity contours for different flap deflections (δ_f) are presented in Figure 15. The comparison of the static pressure contours for zero flap deflection and for the deflected flap at the same angle of attack shows that the flap deflection increases the negative pressure over the entire upper surface of the main airfoil and increases the positive pressure on the lower surface near the trailing edge. The pressure on the lower surface increases rapidly with flap deflection, while the pressure on the upper surface increases gradually. The pressures on both the upper and the lower surfaces of the flap increase with flap deflection.

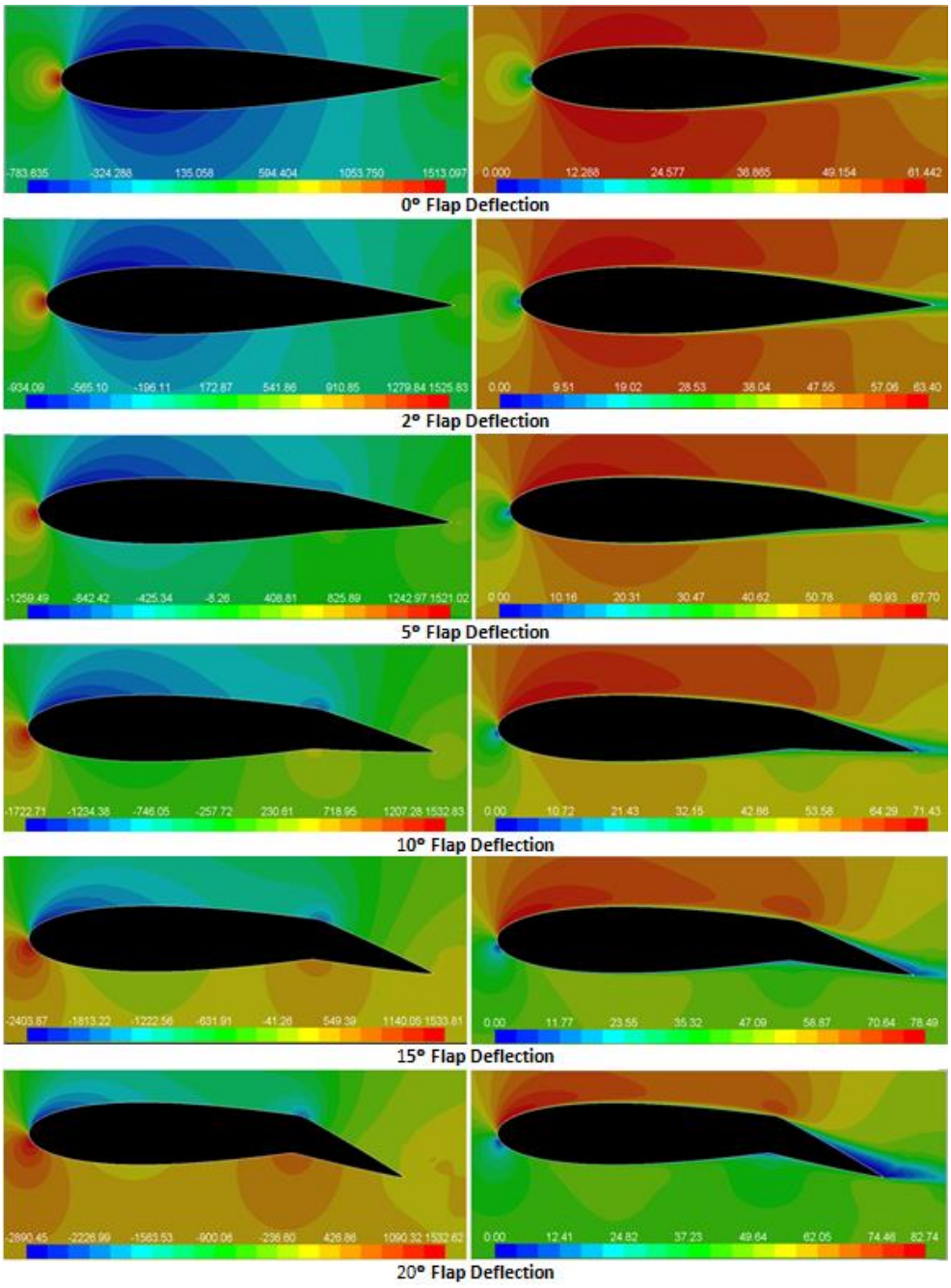

Figure 15. *Cont.*

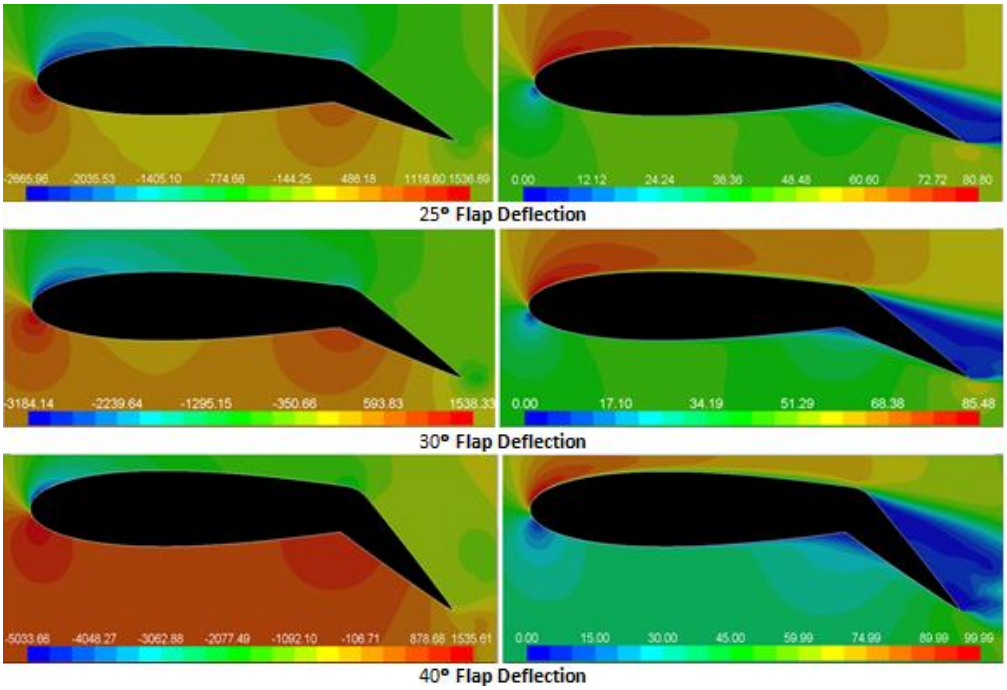

Figure 15. Static pressure and velocity magnitude contours around the NACA 0015 flapped airfoil at an angle of attack of 0° for different flap deflections.

One other interesting observation is the progressive increase of the velocity magnitude over the upper surface of the main airfoil as the flap deflection increases. The flap deflection changes the velocity and pressure distributions on the airfoil upper and lower surfaces, causing higher pressure to be built over the rear portion, generating a net lift force at AoA = 0°, and increases the airfoil maximum lift coefficient. The flap deflection also moves the zero lift angle-of-attack of the airfoil to a lower negative value and greatly increases the drag force.

Figure 16 shows the predicted variation of the lift coefficient with the flap deflection at two different angles of attack of $\alpha = 5°$ and $\alpha = 10°$. Here, the realizable k-ε predictions are compared with the simulation results of Hassan [16] and Luchian [36], as well as the experimental data of Williamson [37]. Hassan [16] studied the aerodynamic performance of the NACA 0015 airfoil with a 25% trailing edge flap at Re = 3×10^6 and for different Mach numbers. Luchian [36] investigated the aerodynamic performance of the NACA 0015 airfoil with a 27.5% trailing edge plain flap for different flap deflection angles at Re = 10^6 by using three different codes (Javafoil 2.20, Martin Hepperle, Braunschweig, Germany, Profili2.20, Stefano Duranti, Feltre, Italy, and XFLR5 6.06, techwinder, Paris, France). Williamson [37] conducted experiments on the W1015 airfoil, which is identical to the NACA 0015 airfoil for wide range of low Reynolds numbers and trailing edge flap deflections. It is evident that the lift coefficient increases sharply with the increase of the flap deflection up to about 10°–15°, and then, the rate of increase becomes slower up to $\delta_f = 40°$. The present model predictions are in general agreement with the results of Hassan [16] for high Reynolds numbers for flap deflections up to $\delta_f = 20°$, the results of Luchian [36] at low Reynold numbers for flap deflections up to $\delta_f = 30°$ and the experimental data of Williamson [37] for low Reynolds numbers for a wide range of flap deflections up to $\delta_f = 40°$.

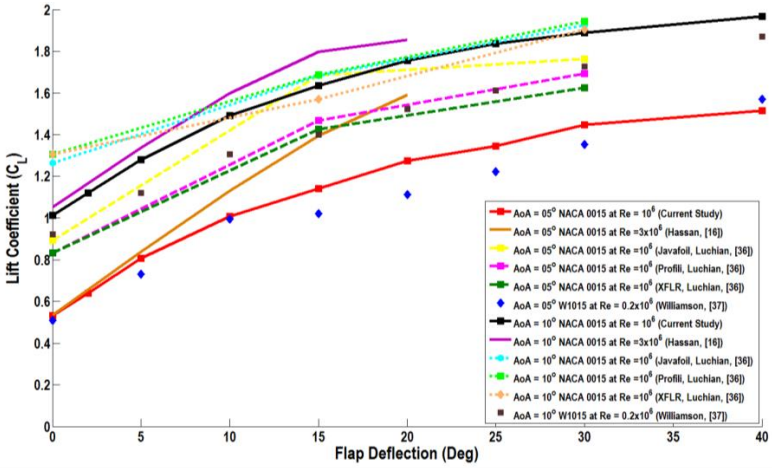

Figure 16. Comparison of effect of flap deflection on lift coefficient for AoA = 5° and AoA = 10° with Hassan's [16] simulations, Luchian's [36] results and Williamson's [37] experiments.

Figure 17 shows the predicted variation of the drag coefficient with the flap deflection at two different angles of attack of $\alpha = 5°$ and $\alpha = 10°$. For $\alpha = 5°$, the drag coefficient of the flapped airfoil increases gradually with the flap deflection up to a flap angle of $\delta_f = 20°$, and then, the rate of increase becomes much shaper. For example, the drag coefficient at $\delta_f = 30°$ is more than two-times its value at $\delta_f = 15°$. The trend is somewhat different for the AoA of $\alpha = 10°$, where the drag coefficient increases gradually with the flap deflection up to $\delta_f = 15°$, and then, the drag coefficient increases sharply. The drag coefficient for $\delta_f = 30°$ in this case is more than five-times its value at ($\delta_f = 10°$). When compared with the earlier results, the drag coefficients obtained by the realizable k-ε model in this study are reasonably accurate for the AoA = 5° and in the entire range of flap deflections up to $\delta_f = 30°$. It is clear that for the AoA = 10° and $\delta_f > 15°$, the predicted drag values are somewhat higher than those predicted by both the Profili and XFLR5 codes, but below the values obtained by the Javafoil code.

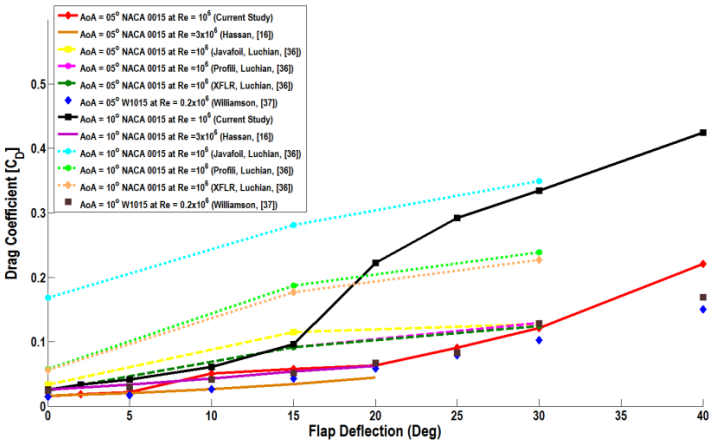

Figure 17. Comparison of the effect of flap deflection on drag coefficient values at AoA = 5° and AoA = 10° with Hassan's [16] simulations, Luchian' [36] results and Williamson's [37] experiments.

The effect of flap deflection on lift increment is presented next. A lift increment ΔC_l is the amount of lift that is gained or lost due to a flap deflection measured from a reference configuration. The airfoil with zero flap deflection is taken as the reference case. The trend in these plots is compared with the experimental data of Williamson [37] for the W1015 symmetrical airfoil tested at Re = 4×10^5 at zero flap deflection and 10° flap deflection.

Figure 18a exhibits the variation of the lift coefficient with the angle of attack at a flap deflection of $\delta_f = 10^\circ$ together with their corresponding reference values at $\delta_f = 0^\circ$. Figure 18b presents an enlarged section of the lift coefficient for small angles of attack. In addition, the increments in the values of the lift coefficient are shown in Figure 18b. It is seen that the lift increment value $\Delta\, C_l$ due to the flap angle is roughly the same for a large range of incidence angles below the stall angle. That is, $(\Delta\, C_l)_1 \cong (\Delta\, C_l)_2$ for the airfoils with zero and 10° flap angle.

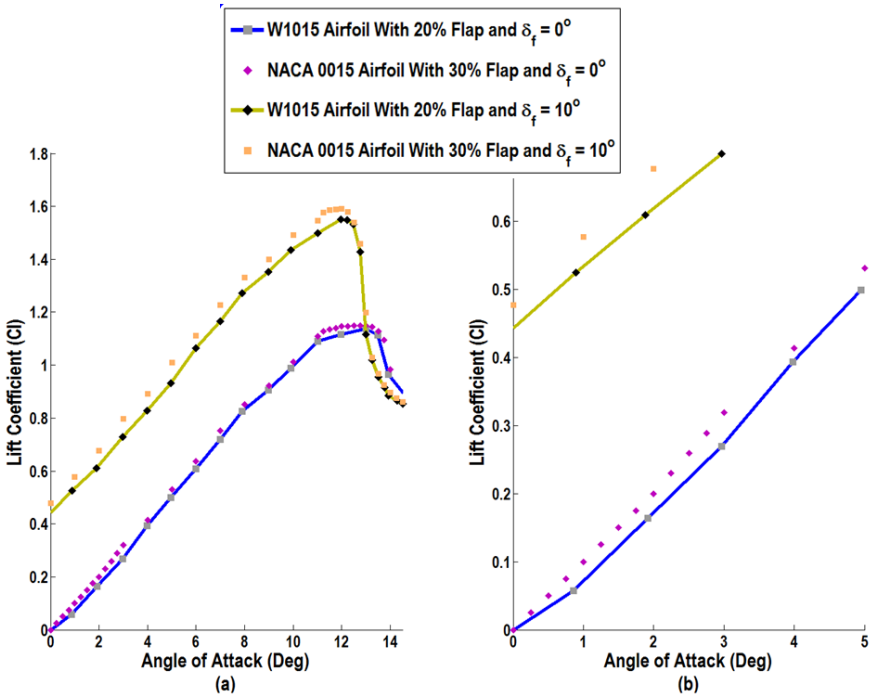

Figure 18. Lift increment at flap deflection of 10° and validation with the experimental data of Williamson [37].

In Figure 18b, it can be seen that at $\delta_f = 0^\circ$, the slope of the lift curve for the W1015 airfoil is slightly lower than the slope of the lift curve for the NACA 0015. It should also be pointed out that the W1015 airfoil was tested at Re = 4×10^5, and the NACA 0015 results are for Re = 10^6. It is also known that for the same angle of attack, a higher Reynolds number gives higher lift coefficient and consequently a greater slope of the lift curve. The lift curves for both airfoils are nearly linear at low angles of attack (below 10°).

Due to the flap deflection, it is observed that the lift coefficient has a nonzero value at zero AoA for both airfoils. For both airfoils, the lift increment is nearly constant at low angles of attack. The lift increment is slightly higher for the NACA 0015 due to the higher Reynolds number for the flow computations. Table 7 shows the values of the increments in the lift coefficient obtained due to a flap deflection of 10° for both airfoils.

Table 7. The Increment in the value of the lift coefficient due to a flap deflection of 10°.

AoA	ΔC_l	ΔC_l
	W1015 (Re = 4×10^5)	**NACA 0015 (Re = 10^6)**
0	0.435	0.477
4.0	0.433	0.476
8.0	0.430	0.463
12.0	0.420	0.441

Simulation results for the lift increment due to flap deflection at zero angle of attack for a wide range of flap deflections are plotted in Figure 19, and the results are compared with the experimental data. There are three distinct regions that define different trends of ΔC_l values. A linear region is observed at smaller flap deflections of $0 \leq \delta_f \leq 15^\circ$. In this region, the slope of the ΔC_l curve is constant, indicating fully-attached flow conditions. The second region is the transitional region, as it acts as a connection between linear and nonlinear regions. It is normally marked as the leveling or decreasing of ΔC_l values that is caused by the separation of flow from the upper surface of the flap. Separation from the upper surface normally occurs around a flap deflection of 10–20 deg. The actual flap deflection for flow separation depends on the Reynolds number, airfoil thickness, flap-chord ratio, angle of attack and the size of the gap around the nose of the flap. The third region is nonlinear in nature due to the reduced nonlinear increase of ΔC_l values with flap deflection. In this region, the flow is largely separated over the upper surface of the flap.

Figure 19 shows that the current realizable k-ε model predictions for the lift increment are in close agreement with the experimental data of Williamson [37]. For flap deflection angles $\delta_f \leq 20^\circ$, it is seen that the lift increment ΔC_l varies linearly in the simulations. The simulations of Hassan [16] were for a high Reynolds number flow and have a linear trend, but a higher slope. For high flap deflections ($\delta_f > 20^\circ$) and a high Reynolds number, Hassan [16] did not provide any data. From Figure 19, it is concluded that the present model predictions are reasonably accurate at least for low Reynolds number flows.

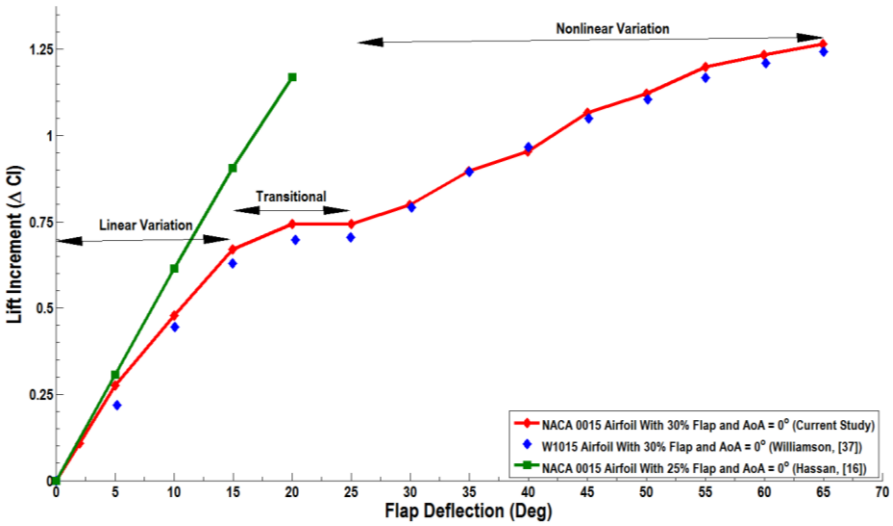

Figure 19. Variation of ΔC_l with flap deflection at zero AoA and comparison with the experimental data of Williamson [34] and simulations of Hassan [16].

It is of interest to study the effect of the flap deflection on both the maximum lift coefficient and the corresponding angle of attack (critical or stall AoA). The variation of the predicted maximum lift coefficient versus flap deflection is shown in Figure 20a, while the variation of the stall angle of attack is illustrated in Figure 20b. In these figures, the corresponding results of Williamson [37] and Hassan [16] are reproduced for comparison. Figure 20a shows that the maximum lift coefficient increases linearly for small flap deflections $0 \leq \delta_f \leq 15^\circ$. For flap deflections larger than 15°, however, the increasing slope of the maximum lift coefficient is reduced and reaches a plateau for the flap deflection in the range of $40^\circ < \delta_f < 60^\circ$. Thus, it can be concluded that deflection of the flap $\delta_f > 40^\circ$ does not provide additional benefit in regard to the maximum lift coefficient. Figure 19a also shows that the trends of the maximum lift coefficient obtained by the present realizable k-ε model are comparable to those of the experimental data of Williamson [37] for the W1015 airfoil, as well as the results of Hassan [16] for

the NACA 0015 airfoil. The magnitudes are, however, somewhat different, and the present simulation results lie in between the results of Williamson [37] and Hassan [16].

Figure 20b shows the variation of the stall angle versus flap angle. It is seen that the current model predictions follow the general trend of the published results, as the stall angle of attack at which $C_{l,\,\max}$ is achieved decreases with increasing the flap deflection. Deflecting the flap by 20° decreases the stall angle of attack by 1.75° in the present study, while leading to a decrease of 1.5° in the experimental study of Williamson [37] and 0.75° in the results of Hassan [16]. The further increase in the flap deflection decreases the stall angle of attack. The present model predicts that lowering the flap by 40° decreases the stall angle of attack by 2°, while Williamson's [37] data suggest a decrease of the stall angle of attack by 4°.

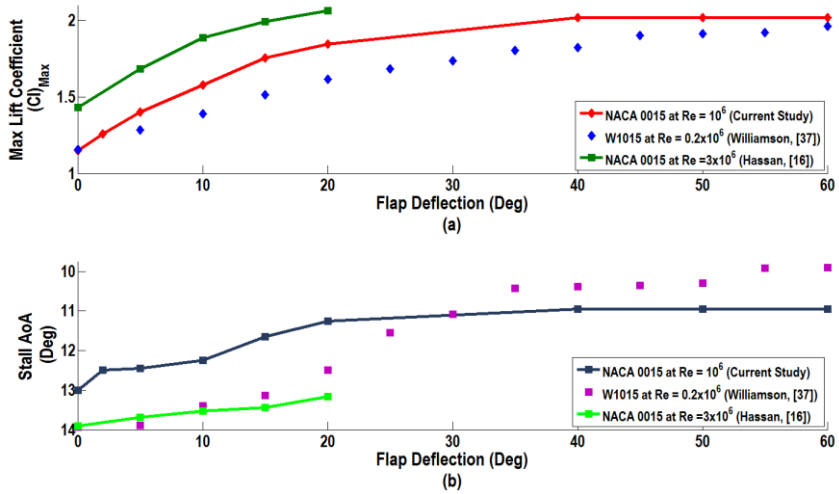

Figure 20. Comparison of effect of flap deflection on (**a**) the maximum lift coefficient and (**b**) the stall angle of attack with the experimental data of Williamson [37] and Hassan [16].

The turbulence intensity contours of the flow around the flapped airfoil at some selected deflection angles and zero incidence are also evaluated. Figure 21 presents the contours of turbulence intensity at δ_f 2°, 5°, 10°, 15°, 20°, 25°, 30° and 40° and for zero incidence angle. It is observed that at the zero incidence angle, the flap deflection has a pronounced influence on the turbulence intensity around the flapped airfoil. Even a small deflection in flap angle disturbs the flow and creates regions of high turbulence intensity in the upper surface of the flapped airfoil. These regions expand with increasing of the flap deflection and shift from the main airfoil towards the flap section. For $\delta_f \leq 15°$, the realizable k-ε model predicts that the peak turbulence intensity occurs in the boundary layer near both the upper and lower surfaces of the main airfoil close to the leading edge and with a lower level of turbulence intensity in the wake region. For $\delta_f \geq 15°$, however, the maximum turbulence intensity occurs in the wake region close to the flap in addition to the boundary layer regions. This is due to the fact that the region with recirculating flow becomes larger as the wake width increases with the flap deflection. At high flap deflections, the flow separates from the flap, and high pressure acting on the pressure side of the flapped airfoil and consequently marked increase in the drag occur compared to situations where the flow remains attach to the surface.

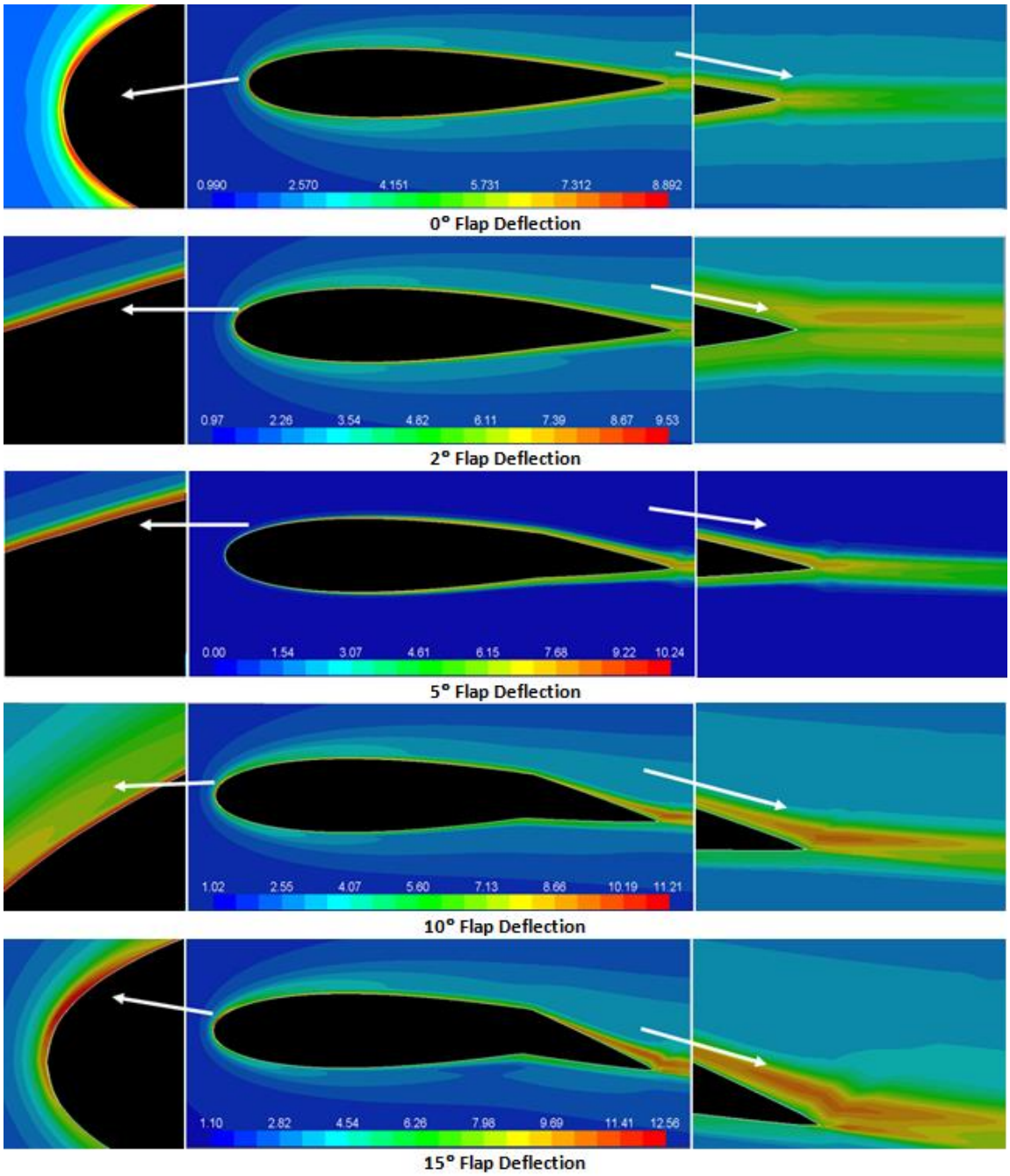

Figure 21. *Cont.*

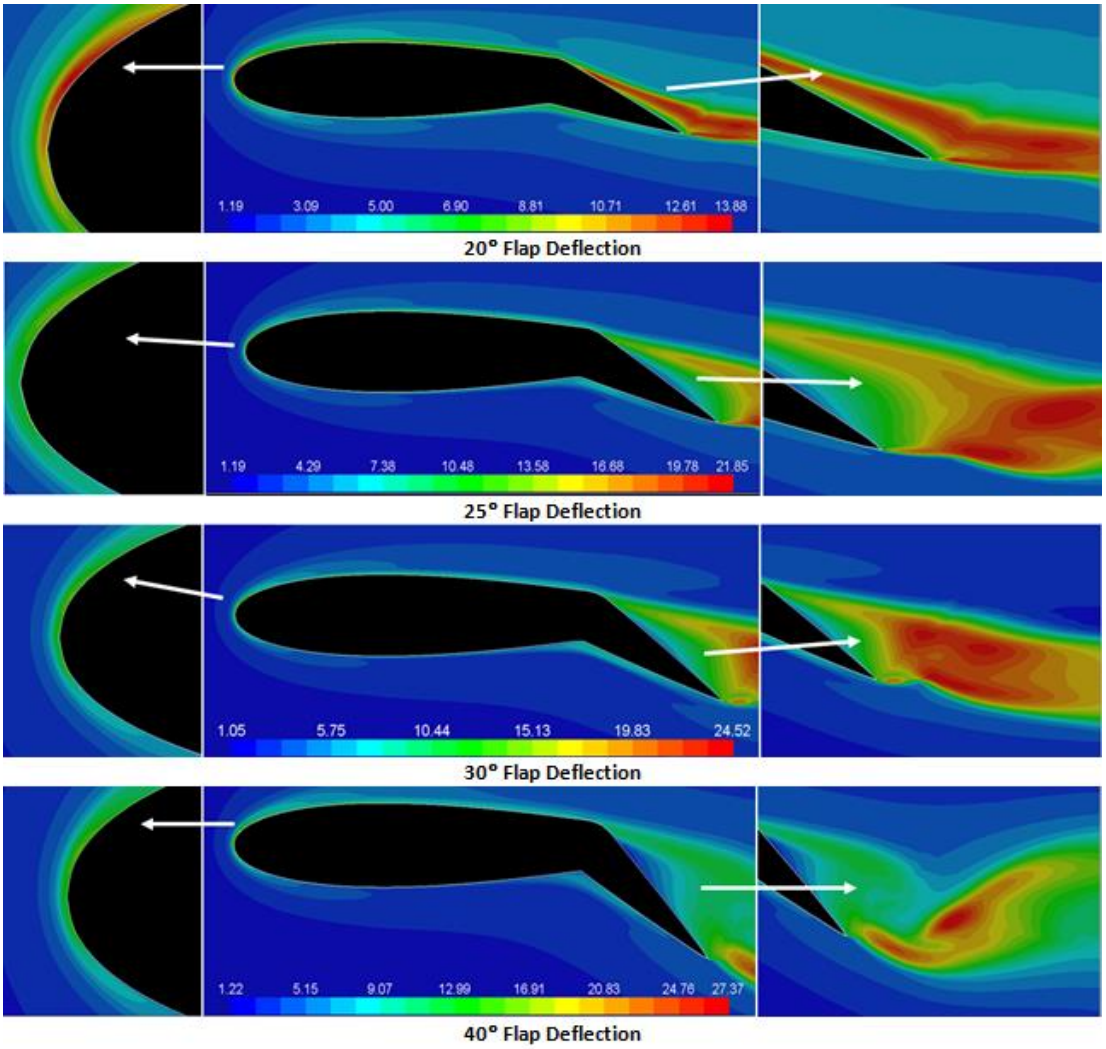

Figure 21. Contours of turbulence intensity (%) around the flapped airfoil at AoA = 0° and various flap deflections.

4. Conclusions

Using the realizable *k*-ε turbulence model, a numerical investigation of flow characteristics over the NACA 0015 airfoil at Re = 10^6 at different flap deflections was conducted. The airfoil with the deflected trailing edge flap was treated as a single element with no gap between the airfoil and the flap leading edge. A parabolic computational domain with 104,000 structured cells along with 10% turbulence intensity at the far-pressure field at its boundaries was used in the analysis. The grid sensitivity was performed to satisfy the mesh independence condition. For different configurations with and without flap deflections, flows over the airfoil were simulated, and the resulting lift and drag coefficients were validated by comparison with earlier experimental data and numerical simulation results. Based on the presented results, the following conclusions are drawn:

- The simulation results showed that the realizable *k*-ε model is a suitable turbulence model for simulating the flow characteristics around an airfoil at different angle of attacks and flap deflections.
- Results showed that the increasing incidence angle was associated with the increasing lift coefficient up to the maximum of 1.15 at $\alpha = 13°$, after which the lift coefficient sharply decreases. Before stall, the slope of the lift versus incidence angle curve, $\frac{\partial C_l}{\partial \alpha}$, remained roughly constant

at about 0.101. After the stall angle of attack, the lift coefficient decreased sharply with further increase of the incident angle, leading to a lift coefficient of 0.79 at $\alpha = 17^\circ$.

- The value of the drag coefficient was low at zero incidence angles and increased slowly with the angle of attack to the value of 0.038 at the stall condition. The slope of the drag versus incidence angle curve, $\frac{\partial C_d}{\partial \alpha}$, remained roughly constant at about 0.003. After the stall condition, the drag increased rapidly with the further increase of the angle of attack to reach a value of 0.28 at $\alpha = 20^\circ$, which was more than seven-times the drag coefficient at the stall condition. The slope of the drag versus incidence angle curve, $\frac{\partial C_d}{\partial \alpha}$, jumped to a value of 0.04 after the stall condition.
- For the case with zero flap deflection, the turbulence intensity around the airfoil increased with incident angle and would reach a maximum of 49% at $\alpha = 20^\circ$.
- The presented results showed that flap deflection significantly affected the aerodynamic performance of the airfoil. For the same angle of attack, increasing δ_f enhanced both the lift and drag coefficients.
- The lift increment (ΔC_l) increased with the flap deflection angle. This trend continued until a maximum value was reached, and then, the lift increment remained constant. The maximum lift coefficient was 2.02 for the range of parameters studied.
- Increased flap deflection moved the zero-lift incidence angle of the airfoil from 0° to negative values. For $\delta_f = 5^\circ$ and $\delta_f = 10^\circ$, the zero-lift incidence angle were, respectively, $\alpha = -1.9^\circ$ and $\alpha = -2.7^\circ$.
- Increased flap deflection decreased the stalling angle of attack (α_{stall}) for which the maximum lift coefficient was reached. The stalled angles of attack were $\alpha = 13^\circ$, 12.25° and 11.25°, respectively, for flap deflections of $\delta_f = 0^\circ$, 10° and 20°.
- For all investigated flap deflections, the slope of the lift versus incidence angle, $\frac{\partial C_l}{\partial \alpha}$, remained roughly constant at about 0.1, and the lift curve just shifts upwards due to increased flap deflection.
- For the zero incident angle, the turbulence level increased with the increase of flap deflection and reached to 27% at $\delta_f = 40^\circ$.

Acknowledgments: The authors gratefully acknowledge the financial support of the U.S. Air Force Office of Scientific Research through Grant No. FA9550-09-1-0051.

Author Contributions: This study was a part of the PhD research work of Sohaib Obeid who was responsible for developing the computational model and for performing the simulations and data analysis. Ratneshwar Jha and Goodarz Ahmadi contributed to the interpretation of the results and to the critical revision of the article.

Conflicts of Interest: The authors declare no conflict of interest.

References

1. Anderson, J.D., Jr. *Fundamentals of Aerodynamics*, 3rd ed.; McGraw-Hill Series in Aeronautical and Aerospace Engineering; McGraw-Hill: New York, NY, USA, 2001; pp. 283–335.
2. You, D.; Moin, P. Active control of flow separation over an airfoil using synthetic jets. *J. Fluids Struct.* **2008**, *24*, 1349–1357. [CrossRef]
3. Schrauf, G. Application of laminar flow technology on transport aircraft. In Proceedings of the CEAS Drag Reduction Conference, Potsdam, Germany, 19–21 June 2000.
4. Günther, B.; Carnarius, A.; Thiele, F. Numerical investigation of active flow control applied to an airfoil with a camber flap. In *Active Flow Control II*; King, R., Ed.; Notes on Numerical Fluid Mechanics and Multidisciplinary Design; Springer: Berlin/Heidelberg, Germany, 2010; Volume 108, pp. 45–61.
5. Ham, N.D. Helicopter individual blade control research at MIT 1977–1985. *Vertica* **1987**, *11*, 109–122.
6. Hall, S.R.; Spangler, R.L., Jr. Piezoelectric Helicopter Blade Flap Actuator. US Patent 5,224,826, 6 July 1993.
7. Hall, S.R.; Prechtl, E.F. Development of piezoelectric servo-flap for helicopter rotor control. *Smart Mater. Struct.* **1996**, *5*, 26–34. [CrossRef]
8. Chopra, I. Status of application of smart structures technology to rotorcraft systems. *J. Am. Helicopter Soc.* **2000**, *45*, 228–252. [CrossRef]

9. Hall, S.R.; Wereley, N.M. Performance of higher harmonic control algorithms for helicopter vibration reduction. *AIAA J. Guid. Control Dyn.* **1993**, *16*, 794–797. [CrossRef]
10. Van Kuik, G. The application of smart structures for large wind turbine rotor. In Proceedings of the 50th IEA Topical Expert Meeting, Delft University of Technology, Delft, The Netherland, 11–12 December 2006.
11. Somers, D.M. *Effect of Flap Deflection on Section Characteristics of S813 Airfoil (Period of Performance: 1993–1994)*; NREL/SR-500–36335; National Renewable Energy Laboratory: Golden, CO, USA, 2005.
12. McCroskey, W.J. *A Critical Assessment of Wind Tunnel Results for the NACA 0012 Airfoil*; NASA Technical Memorandum 100019; NASA Technical Reports Server (NTRS): Hampton, VA, USA, 1989.
13. Little, J.; Samimy, M. High-Lift airfoil separation with dielectric barrier discharge plasma actuation. *AIAA J.* **2010**, *48*, 2884–2898. [CrossRef]
14. Gerakpoulos, R.; Boutier, M.S.H.; Yarusevych, S. Aerodynamic characteristics of NACA 0018 airfoil at low reynolds numbers. In Proceedings of the 40th Fluid Dynamic Conference and Exhibit, Chicago, IL, USA, 28 June–1 July 2010.
15. Gault, D.E. *A Correlation of Low-Speed, Airfoil-Section Stalling Characteristics with Reynolds Number and Airfoil Geometry*; NACA Technical Note 3963; NACA Technical: Washington, DC, USA, 1957.
16. Hassan, A. *Predicted Aerodynamic Characteristics of a NACA 0015 Airfoil Having a 25% Integral Type Trailing Edge Flap*; NACA CR/-1999–209328; NASA Technical Reports Server (NTRS): Hampton, VA, USA, 1999; pp. 209–328.
17. Zhang, G.; Jiang, J.; Liu, C. Numerical simulation of aerodynamic performance for wind turbines. *J. East China Electric Power* **2009**, *37*, 449–452.
18. Srinivasan, G.R.; Ekaterinaris, J.A.; McCroskey, W.J. Evaluation of turbulence models for unsteady flows of an oscillating airfoil. *Comput. Fluids* **1995**, *24*, 833–861. [CrossRef]
19. Menter, F.R. *Best Practice: Scale-Resolving Simulations in ANSYS CFD, Version 1*; ANSYS Germany GmbH, Inc.: Canonsburg, PA, USA, 2012; pp. 3–5.
20. Shih, T.H.; Liou, W.W.; Shabbir, A.; Yang, Z.; Zhu, J. A new k-ε eddy viscosity model for high reynolds number turbulent flows. *Comput. Fluids* **1995**, *24*, 227–238. [CrossRef]
21. Kim, S.E.; Choudhury, D.; Patel, B. Computations of complex turbulent flows using the commercial code FLUENT. In Proceedings of the ICASE/LaRC/AFOSR Symposium on Modeling Complex Turbulent Flows, Hampton, VA, USA, 11–13 August 1997; pp. 259–276.
22. Dolle, T.J.A. Flap Performance Improvement by Surface Excitation. Master's Thesis, Aerospace Engineering, Delft University of Technology, The Netherlands, 2009; pp. 23–27.
23. ANSYS, Inc. *Introduction to ANSYS FLUENT 12.0. "Lecture 5 Solver Setting" ANSYS, Release 13*; ANSYS, Inc.: Canonsburg, PA, USA, 2010; pp. 8–30.
24. Anderson, W.K.; Bonhaus, D.L. An implicit upwind algorithm for computing turbulent flows on unstructured grids. *Comput. Fluids* **1994**, *23*, 1–21. [CrossRef]
25. Bakker, A. *Lecture 5—Solution Methods Applied Computational Fluid Dynamics*; Lectures of Fluent Instructor; Fluent Inc.: New York, NY, USA, 2002; pp. 41–43.
26. Spalart, P.; Allmaras, S. A one-equation turbulence model for aerodynamic flows. In Proceedings of the 30th Aerospace Sciences Meeting and Exhibit, Aerospace Sciences Meetings, Reno, NV, USA, 6–9 January 1992.
27. Rethmel, C.C. Airfoil Leading Edge Flow Separation Control Using Nanosecond Pulse DBD Plasma Actuators. Master's Thesis, Mechanical Engineering, The Ohio State University, Columbus, OH, USA, 2011; pp. 25–30.
28. Ahmed, T.; Amin, M.T.; Islam, S.M.R.; Ahmed, S. Computational study of flow around a NACA 0012 wing flapped at different flap angles with varying mach numbers. *Glob. J. Res. Eng. Gen. Eng.* **2013**, *13*, 4–16.
29. Joslin, R.D.; Horta, L.G.; Chen, F.J. Transiting action control to application. In Proceedings of the 30th AIAA Fluid Dynamics Conference, Norfolk, VA, USA, 28 June–18 July 1999.
30. Lasse, G.; Niels, S. Large eddy simulations of an airfoil in turbulent inflow. In *4th PhD Seminar on Wind Energy in Europe: Book of Abstracts*; The European Wind Energy Association: Brussels, Belgium, 2008; pp. 33–36.
31. Joseph, D.D.; Funada, T.; Wang, J. *Potential Flows of Viscous and Viscoelastic Fluids*; Notes to Fluid Mechanics Students; University of Minnesota: Minneapolis, MN, USA, 2010; pp. 1–25.
32. Schroeder, E.J. Low Reynolds Number Flow Validation Using Computational Fluid Dynamics with Application to micro Air Vehicles. Master's Thesis, Aeronautical Engineering, University of Maryland, College Park, MD, USA, 2005; pp. 20–23.

33. Sharma, D.M. Experimental Investigations of Dynamic Stall for an Oscillating Airfoil. Ph.D. Thesis, Aeronautical Engineering, Indian Institute of Technology Kanpur, Kanpur, India, 2010; pp. 90–102.
34. Sheldahl, R.E.; Klimas, P.C. *Aerodynamic Characteristics of Seven Symmetrical Airfoil sections Through 180 Degree Angle of Attack for Use in Aerodynamic Analysis of Vertical Axis Wind Turbines*; Sandia National Laboratories: Albuquerque, NM, USA, 1981; pp. 20–36.
35. Şahin, I.; Acir, A. Numerical and experimental investigations of lift and drag performances of NACA 0015 wind turbine airfoil. *Int. J. Mater. Mech. Manuf.* **2015**, *3*, 22–25. [CrossRef]
36. Luchian, A. Numerical and Experimental Study on the Effect of High Lift Devices on NACA 0015 Aerodynamics. Ph.D. Thesis, Mechanical Engineering, Polytechnic University of Bucharest, Bucharest, Romania, 2014; pp. 54–61.
37. Williamson, G.A. Experimental Wind Tunnel Study of Airfoils with Large Flap Deflections at Low Reynolds Numbers. Master's Thesis, Aerospace Engineering, The University of Illinois at Urbana-Champaign, Champaign, IL, USA, 2012; pp. 14–60.